Journal of Volcanology and Geothermal Research 306 (2015) 17–40

Contents lists available at ScienceDirect

Journal of Volcanology and Geothermal Research

journal homepage: www.elsevier.com/locate/jvolgeores

A complex magma reservoir system for a large volume intra- to extra-caldera ignimbrite: Mineralogical and chemical architecture of the VEI8, Permian Ora ignimbrite (Italy)

M.A.W. Willcock [a,*], G.M. Bargossi [b], R.F. Weinberg [a], G. Gasparotto [b], R.A.F. Cas [a], G. Giordano [c], M. Marocchi [b,1]

[a] School of Earth, Atmosphere and Environment, Monash University, Clayton, VIC 3800, Australia
[b] Dipartimento di Scienze della Terra e Geologico-Ambientali, Università di Bologna, Piazza Porta San Donato, 1-40126 Bologna, Italy
[c] Dipartimento di Scienze Geologiche, Università di Rome Tre, Lago S. Leonardo Murialdo 1, 00146 Rome, Italy

A R T I C L E I N F O

Article history:
Received 13 April 2015
Accepted 4 September 2015
Available online 25 September 2015

Keywords:
Ora caldera
Northern Italy
Ignimbrite
Intra-caldera setting
Rhyolite
Caldera eruption dynamics

A B S T R A C T

Intra-caldera settings record a wealth of information on caldera-forming processes, yet field study is rarely possible due to lack of access and exposure. The Permian Ora Formation, Italy, preserves >1000 m of vertical section through its intra-caldera succession. This provides an excellent opportunity to detail its mineralogical and geochemical architecture and gain understanding of the eruption evolution and insight into the pre-eruptive magma system. Detailed juvenile clast phenocryst and matrix crystal fragment point count and image analysis data, coupled with bulk-rock chemistry and single mineral compositional data, show that the Ora ignimbrite succession is rhyolitic (72.5–77.7% SiO_2), crystal-rich (~25–57%; average 43%) and has a constant main mineral population (volcanic quartz + sanidine + plagioclase + biotite). Although a seemingly homogeneous ignimbrite succession, important subtle but detectable lateral and vertical variations in modal mineralogy and bulk-rock major and trace elements are identified here.

The Ora Formation is comprised of multiple lithofacies, dominated by four densely welded ignimbrite lithofacies. They are crystal-rich, typically lithic-poor (<2%), and juvenile clast-bearing (average 20%). The ignimbrite lithofacies are distinguished by variation in crystal fragment size and abundance and total lithic content. The intra-caldera stratigraphic architecture shows both localised and some large-scale lithofacies correlation, however, it does not conform to a 'layer-cake' stratigraphy. The intra-caldera succession is divided into two depocentres: Southern and Northern, with proximal extra-caldera deposits preserved to the south and north of the system.

The Southern and Northern intra-caldera ignimbrite successions are discriminated by variations in total biotite crystal abundance. Detailed mineralogical and chemical data records decreases across the caldera system from south to north in biotite phenocrysts in the groundmass of juvenile clasts (average 12–2%), matrix biotite (average 7.5–2%) and plagioclase crystal fragments (average 18–6%), and total crystal fragment abundance in the matrix (average 47–37%); a biotite compositional change to iron-rich (0.57–0.78 Fe); and bulk-rock element decreases in Fe_2O_3, MgO, P_2O_5, Ce, Hf, V, La and Zr, and increases in SiO_2, Y and Nb, with TiO_2. Together, the changes enable subtle distinction of the Southern and Northern successions, indicating that the Northern deposits are more evolved. Furthermore, the data reveals discrimination within the Northern succession, with the northwestern extra-caldera fine-crystal-rich lithofacies, having a distinct texture, componentry and composition.

The componentry variation, mineralogical and chemical ranges identified here are consistent with an eruption from a heterogeneous magma system. Our results suggest that the Ora magma was likely stored in multiple chambers within a genetically related magma reservoir network. The mineralogical and chemical architecture together with stratigraphic relationships, enable interpretation of eruption sequence. Caldera eruption is proposed to have commenced in the south and progressed to the north, forming the two pene-contemporaneous caldera depressions. Moreover, this data illustrates heterogeneity and local zonation from base-to-top of the main intra-caldera and extra-caldera successions. These variations together with crystal fragment size variations between ignimbrite lithofacies support the hypothesis of a multi-vent eruption process, incremental caldera in-filling by subtly compositionally different pyroclastic flow pulses, and a lower intensity eruption style (Willcock et al., 2013, 2014).

* Corresponding author at: School of Earth, Atmosphere and Environment, P.O. Box 28E, Monash University, Clayton, Victoria 3800, Australia.
E-mail address: madelainewillcock@gmail.com (M.A.W. Willcock).

[1] Deceased.

http://dx.doi.org/10.1016/j.jvolgeores.2015.09.015
0377-0273/

1. Introduction

Caldera volcano research is becoming ever more important as volcanic eruptions – even relatively small ones e.g. the 2010 Eyjafajallajokull eruption, Iceland (Gudmundsson et al., 2010) – are having greater impacts on society and the natural environment (Lipman, 2000; Bindeman, 2006). Understanding the very large active caldera systems, such as Yellowstone, USA (Girard and Stix, 2012), and Toba, Indonesia (Chesner, 2012), is paramount. Of the many unknown questions relating to calderas, the magma reservoir(s) (e.g. Smith and Bailey, 1966; Houghton et al., 1995; Bachmann et al., 2002; Jellínek and DePaolo, 2003; Hildreth, 2004; Bachmann and Bergantz, 2006, 2008; de Silva and Gosnold, 2007; Lipman, 2007; Huber et al., 2012; Cashman and Giordano, 2014), and eruption process (e.g. Druitt and Sparks, 1984; Lindsay et al., 2001; Maughan et al., 2002; Gravley et al., 2007; Hildreth and Wilson, 2007; Wolff et al., 2011; Cas et al., 2012; Ellis and Wolff, 2012; Gregg et al., 2012) are current foci of much research.

The intra-caldera succession is particularly useful as it can provide a more complete record of pre-eruptive magma genesis and caldera collapse, together with eruption and ignimbrite emplacement processes (Lipman, 1984). Access to the intra-caldera in active or recently active systems is generally not possible. When a deposit is sufficiently eroded, it may still be hard to access or too altered to study thoroughly. Therefore, well preserved, accessible intra-caldera deposits are scarce, e.g. Timber Mountain caldera, USA (Lipman, 1976, 1984; Christiansen et al., 1977), Stillwater Volcanic Complex, USA (John, 1995), Caetano Tuff, USA (John et al., 2008; MacDonald et al., 2012), Borrowdale Volcanic Group, United Kingdom (Beddoe-Stephens and Millward, 2000), or the Late Devonian to Permian calderas in Southern Australia (McPhie, 1986; Cas et al., 2003). The Permian Ora caldera in northern Italy, represents a little studied, large volume (>1000 km^3) rhyolitic caldera. Its excellent cross-sectional preservation of the intra-caldera fill presents a rare opportunity to detail the compositional architecture and processes of a major caldera-forming eruption. The Ora Formation records an extremely large caldera eruption, having a minimum erupted volume of >1290 km^3, an outcropping area of approximately 1500 km^2, and a host caldera with dimensions of ~42 × 40 km (Fig. 1c; Willcock et al., 2013). It records the last eruptive event of five major ignimbrite eruptions of the Athesian Volcanic Group, otherwise known as the Atesina Volcanic Complex (e.g. Barth et al., 1993; Bargossi et al., 2007; Marocchi et al., 2008), suggesting the incremental assembly of a batholithic scale magma system, comparable, for example, to the active Toba caldera system in Indonesia (Knight et al., 1986; Gardner et al., 2002; Chesner, 2012).

Initial examination of the Ora ignimbrite succession shows a broadly homogenous deposit, not uncommon for large ignimbrites which frequently have little apparent component or compositional variation. However, the apparent homogeneity can be deceptive and deposits vary from truly alike deposits known as 'monotonous intermediates' (Hildreth, 1981), e.g. the Fish Canyon Tuff (Bachmann and Bergantz, 2003; Bachmann et al., 2005; Charlier et al., 2007), Great Basin Province ignimbrites such as the Lund Tuff, Wah Wah Springs Tuff, Cottonwood Wash Tuff and Monotony Tuff (Ekren et al., 1971; Hildreth, 1981; Best et al., 1989; Maughan et al., 2002; Best et al., 2013), to those where trace elements and/or phenocryst populations, reveal subtle variation, e.g. the Bishop Tuff (Hildreth, 1979; Palmer et al., 1996; Wilson and Hildreth, 2003), ignimbrites of the Yellowstone caldera (Christiansen, 2001) and the Toba Tuff (Chesner, 1998). The aim of this paper is to present componentry, mineralogical and bulk-rock geochemical data to establish if the intra-caldera ignimbrite is indeed homogeneous, or if it shows compositional and mineralogical variations that can be used to understand the evolution of the Ora caldera eruption, the way the caldera was infilled, and the nature of the pre-eruptive magma system. Additionally, this study adds to the body of evidence on large caldera eruption processes.

2. Geological and geochemical background

The Ora Formation is the youngest (277 ± 2–274.1 ± 1.6 Ma; Marocchi et al., 2008) and best exposed eruptive unit of the Athesian Volcanic Group (285.4 ± 1.6–274.1 ± 1.6 Ma; Marocchi et al., 2008), located in the Southern Alps, northern Italy (Fig. 1). The entire Athesian Volcanic Group system formed in a continental setting, which was intermittently active over a 10 Myr period. There was a marked increase in eruption volume and frequency in the latter stages, which produced several large-volume rhyodacitic–rhyolitic ignimbrites (Table 1). The system also comprises subordinate andesitic–rhyolitic lavas and domes and minor epiclastic sedimentary material (Bargossi et al., 2004, 2007; Morelli et al., 2007; Schaltegger and Brack, 2007; Visoná et al., 2007; Marocchi et al., 2008). The Athesian Volcanic Group and the surrounding Permian intrusions are bounded by the Periadriatic lineament to the north and the Valsugana line to the south (Fig. 1b).

Magmatism occurring across Europe during the early Permian (e.g. Marti, 1991; Larsen et al., 2008) resulted from the collapse of the major Hercynian–Variscan orogenic belt and closure of the Palaeo-Tethys ocean (McCann, 2008; Cassinis et al., 2012). These events caused large-scale lithospheric thinning, basin formation, and thermal variability, resulting in many intrusive and extrusive magmatic events across Europe, including the Athesian Volcanic Group (Timmerman, 2004; Plant et al., 2005; Cassinis and Perotti, 2007; Marocchi et al., 2008; McCann et al., 2008; Timmerman, 2008). Importantly, the Athesian Volcanic Group succession has been influenced by the later Triassic marine transgression in the region, which leads to widespread hydrothermal fluid circulation, detected in the Athesian Volcanic Group rocks by shifts in geochemical and isotopic signatures (D'Amico and Del Moro, 1988; Barth et al., 1993; Rottura et al., 1998b). Previously published works on the Athesian Volcanic Group have focussed on the general stratigraphy and geochemical and isotopic characteristics as a whole (D'Amico et al., 1980; Bargossi et al., 1983, 1999, 2004, 2007; Berger and Satir, 1991; Barth et al., 1993; Bonin et al., 1993; Barth, 1994; Rottura et al., 1997, 1998a,b; Timmerman, 2004). These studies show a clear compositional change from a less evolved, lower Athesian Volcanic Group eruptive sequence (andesitic–rhyodacitic), to a more evolved upper Athesian Volcanic Group eruptive sequence (rhyolitic; Table 1), common of many long-lived silicic systems globally (Lipman et al., 1970; Lipman, 2007). Using samples primarily from the Ora ignimbrite, Barth et al. (1993) proposed that these magmas evolved in a compositionally zoned upper crustal magma chamber, inferred from moderate gradients of the major and trace elements and crossover of REE patterns (Barth et al., 1993).

2.1. The Ora Formation

Willcock et al. (2013) suggested that the Ora caldera was a volcano-tectonic system based on the following: the extensional basin environment during the Permian and the multiple prior caldera forming events of the Athesian Volcanic Group, together with the absence of the typical caldera eruption process (lack of a Plinian precursor eruption phase).

The succession is dominated by densely welded ignimbrite deposits (>1 km thickness in total; Willcock et al., 2013; Willcock and Cas, 2014), which are mostly confined within two intra-caldera depressions, Northern and Southern (capitals used here to distinguish the calderas, from general cardinal directions) separated by an intra-caldera ridge (Fig. 1c). Subordinate extra-caldera or outflow deposits are preserved up to 17 km from the margins of the complex correlated on the basis of field, petrographic and geochemical characteristics (<230 m thickness; Fig. 1c). This exceptionally well-exposed Permian ignimbrite succession is widely devitrified and shows some degree of alteration in places, yet remarkably still preserves local primary glassy domains (vitrophyre), primary welding textures (Willcock and Cas, 2014), and moreover, has been relatively unaffected by the later major Alpine orogenies (Bonin et al., 1993; Ring and Richter, 1994; Castellarin and

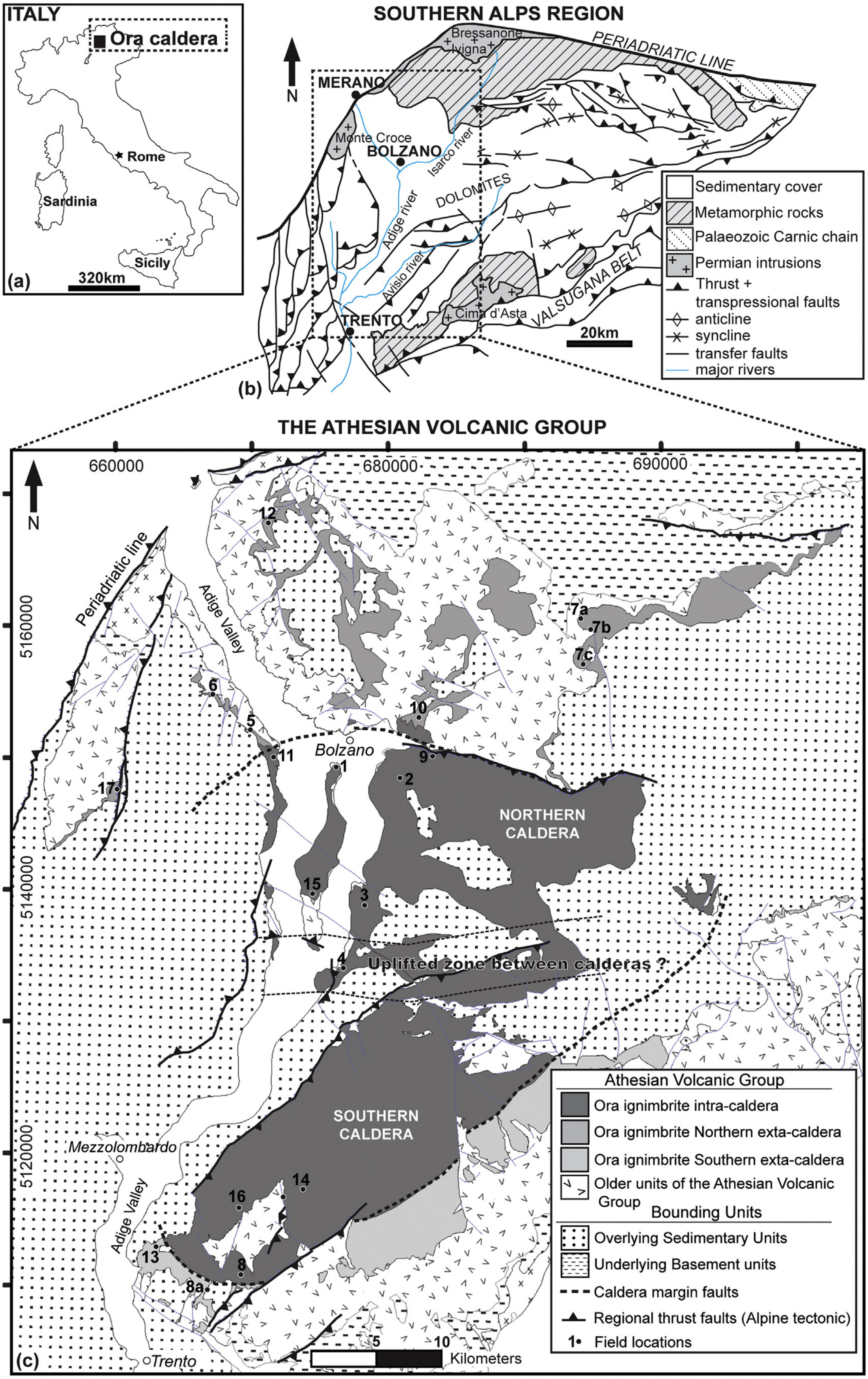

Fig. 1. (a) Location of the Ora caldera complex in northern Italy. (b) Schematic geological map of the Southern Alps region (modified from Castellarin and Cantelli, 2000). (c) Detailed geologic map of the Ora Formation ignimbrite and Athesian Volcanic Group (map modified from Italian geological map 1:50,000, and unpublished data of Bargossi, G.M., Morelli, C. and Piccin, G). Field locations are indicated.

Table 1
Stratigraphic sequence of the Athesian Volcanic Group, together with the new classification of the Ora Formation.

ATHESIAN VOLCANIC GROUP STRATIGRAPHY Modified from Marocchi et al. 2008			
Age (Ma) (U-Pb) zircon	**Unit**	**Lithofacies**	**(m)**
Val Gardena continental sandstone			
~~			
274.1 ± 1.6	ORA_1 Predonico member	Rhyolitic ignimbrite & vitrophyre	250
277 ± 2	ORA formation *refer* ✩	Rhyolitic ignimbrites	800
274.6 ± 2.1	Andriano formation	Rhyolitic lavas	
	Tregiovo formation	Epiclastic material	
276.9 ± 2.3	Gries formation	Rhyolitic ignimbrites	
CALDERA COLLAPSE 2 – Central sector			
	Guncina formation	Epiclastic material	
276.7 ± 1.1	Nalles formation	Rhyolitic ignimbrites	500
CALDERA COLLAPSE 1 – SE sector			
	Verano formation	Epiclastic material	
	Avelengo formation	Rhyodacitic lavas	
276.5 ± 1.1	Gargazzone formation	Rhyodacitic ignimbrites	900
	Castel Leone formation	Rhyodacitic ignimbrites & lavas	
	Sarentino formation	Andesitic lavas & surges	
278.4 ± 1.5 281.5 ± 0.7	Monte Luco formation	Rhyodacitic lavas (minor ignimbrites)	
284.9 ± 1.6	Basal conglomerates	Alluvial conglomerates & sandstones	
~~			
Variscan metamorphic basement			

✩ *THE ORA FORMATION (current study)*				
Member	**Lithofacies**	**Sub-facies**	**Distribution**	**(m)**
ORAd	*Eutaxitic, massive, poorly sorted, fine-crystal-rich, lapilli-tuff (FCLT)*		E (nw)	~ 80
	Eutaxitic, massive, poorly sorted, lithic-rich, lapilli-tuff		E (nw)	
ORAc	*The dominant eutaxitic, massive, poorly sorted, coarse-crystal-rich, lapilli-tuff (CCLT)*		N,S,E (n, ne, nw)	~ 1500
		Bimodal crystal	N,S	
	Eutaxitic, massive, poorly sorted, vitrophyric, lapilli-tuff		N,E (n, ne)	
	Eutaxitic, massive, poorly sorted, lithic-rich, lapilli-tuff		N,S	
	Eutaxitic, massive, poorly sorted, fine-crystal-rich, lapilli-tuff		N	
	Planar stratified, moderately sorted, fine lapilli to coarse tuff		S	
ORAb	*Eutaxitic, massive, poorly sorted, lithic-rich, lapilli-tuff (LRLT)*		N	~ 80
	Planar stratified, poorly sorted, coarse tuff		N	
	Non-planar-stratified, poorly sorted, lithic-rich, fine lapilli to coarse tuff		N	
	Diffusely stratified, moderately lithic-rich, fine tuff		N, S	
ORAa	*Poorly sorted, volcanic lithic breccia (VB)*		N	~ 50
ORA CALDERA COLLAPSE (South to North)				

* N = Northern intra-caldera, S = Southern intra-caldera, E = Extra-caldera: n = northern, ne = north-eastern, and nw = north-western.
Italicized lithofacies represent the main lithofacies of the member, ~~ unconformable bounding contacts of the AVG.

Cantelli, 2000). In general the ignimbrite succession is crystal-rich (~ 25–57%), lithic-poor (generally < 1.5%), with an average of 20% juvenile clasts (Willcock et al., 2013). Although largely devitrified, the Ora succession is the lowest greenschist metamorphic facies, and since it still preserves most original textures, it is amenable to geochemical study and analysis.

The Ora Formation comprises four members (ORAa–ORAd; Table 1; Willcock et al., 2013), including: local volcanic lithic breccia (ORAa), and four ignimbrite lithofacies, with minor local interbedded surge (members ORAb–d; Table 1). A key feature of the Ora Formation is the absence of a Plinian fallout deposit at the base of the ignimbrite succession. The four ignimbrite lithofacies are very similar and have been separated primarily by variation in crystal fragment size and abundance, and total lithic content. *Juvenile clasts* are here defined as fragments of the erupting magma, explosively ejected during the eruption. The crystal components of the ignimbrite are here divided into two categories;

crystal fragments, those crystals liberated from the magma during eruption, now residing as individual crystals within the matrix, and *phenocrysts*, crystals residing within the groundmass of juvenile clasts. Some of the four ignimbrite lithofacies locally recur through the larger succession (Willcock et al., 2013; Table 1), however, the general lithofacies order from base to top includes:

a) basal volcanic lithic lag breccia,
b) eutaxitic, lithic-rich lapilli-tuff,
c) eutaxitic, vitrophyre lapilli-tuff,
d) eutaxitic, coarse-crystal-rich lapilli-tuff, which has a bimodal crystal size sub-facies,
e) eutaxitic, fine-crystal-rich lapilli-tuff.

Significantly, the dominant coarse-crystal-rich lapilli-tuff lithofacies is found in both the Northern and Southern caldera depressions, with field observations enabling general distinction between the two in relation to total biotite crystal fragment abundance (Fig. 2), explored further in Section 4. These lithofacies have been proposed by Willcock et al. (2013) using the most complete Northern caldera succession, to define the main eruption phases: (1) caldera collapse and vent opening, which produced the volcanic lithic lag breccia deposits; (2) vent clearing, preserved by the main deposits of the lithic-rich lapilli tuff lithofacies at the base of ignimbrite succession; (3) waxing and steady eruption, recorded by thick coarse-crystal-rich lapilli-tuff lithofacies deposits, with local basal vitrophyre lapilli-tuff lithofacies deposits; and (4) waning eruption phases; preserved by the main deposits of the fine-crystal-rich lapilli-tuff lithofacies in the north-western outflow succession.

The stratigraphic architecture of the intra-caldera succession reveals a lack of uniformity between the two depo-centres or within each depo-centre. However, some local and wider correlation is possible, such as at the caldera margins (Willcock et al., 2013). The stratigraphic architecture of the Ora ignimbrite has been taken to indicate progressive in-filling of the caldera system from multiple vents and late-stage outflow of material into the extra-caldera setting (Willcock et al., 2013, 2014).

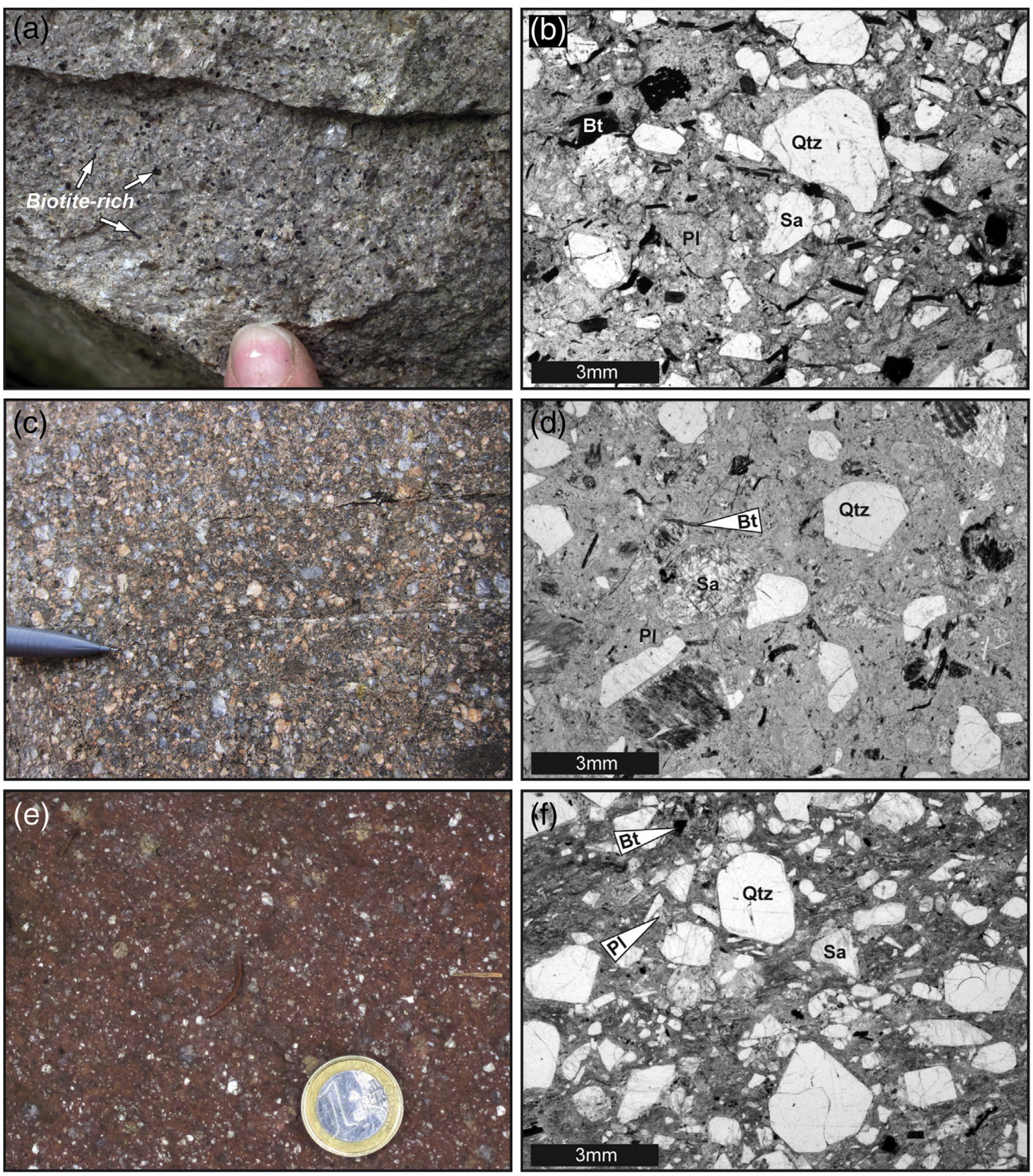

Fig. 2. Field photographs and photomicrographs illustrating ignimbrite deposit variation across the caldera system in relation to visible biotite matrix crystal fragment content. (a–b) Biotite-rich Southern intra-caldera succession (coarse-crystal-rich lapilli-tuff lithofacies, location 14). (c–d) The low-moderately biotite abundant Northern intra-caldera succession (coarse-crystal-rich lapilli-tuff lithofacies, location 2). (e–f) Biotite-poor, northern extra-caldera succession (coarse-crystal-rich lapilli-tuff lithofacies, location 12).

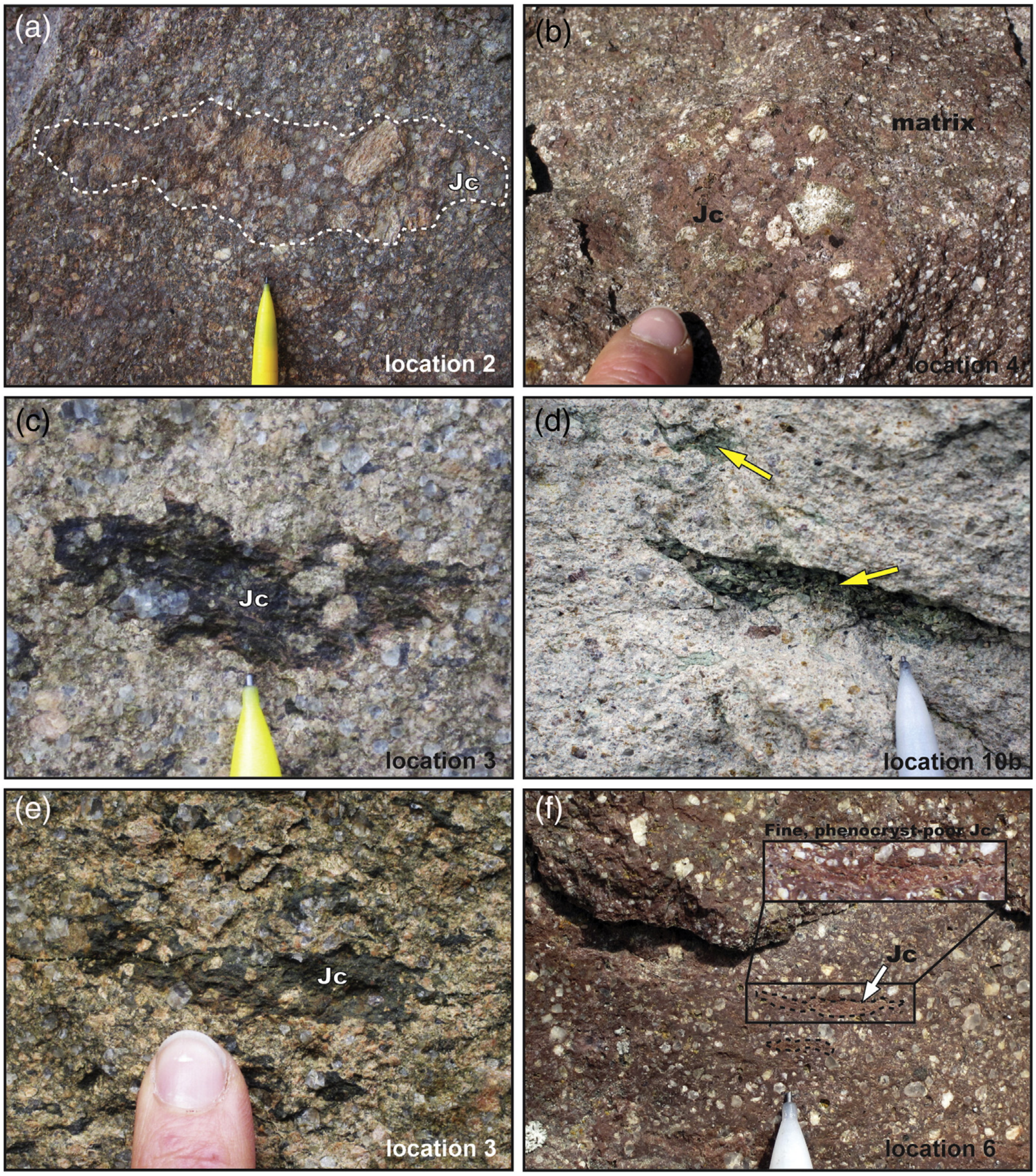

Fig. 3. Variation in juvenile clast type (based on phenocryst size), size, shape and abundance within the ignimbrite succession. (a) Very coarse juvenile clast type (coarse-crystal-rich lapilli-tuff lithofacies). (b–d) Coarse juvenile clast type (in both the lithic-rich and coarse-crystal-rich lapilli-tuff lithofacies). Note the crystal-rich and argyllic altered clasts in (d) shown by arrows (lithic-rich lapilli tuff lithofacies). (e) Medium juvenile clast type (lithic-rich lapilli tuff lithofacies). (f) Fine juvenile clast type (fine-crystal-rich lapilli-tuff lithofacies).

2.2. The Ora caldera eruption

How the collapse of the magma chamber roof block is accommodated during caldera collapse has been of keen interest to researchers in recent times (e.g. Roche and Druitt, 2001; Cole et al., 2005; de Silva et al., 2006; Acocella, 2008; Gregg et al., 2012). Outward or steeply dipping faults have been suggested to facilitate the larger end member eruptions, as they are free to collapse to the base of the system, leading to a large erupted volume fraction (Gudmundsson, 2008). There are several features that suggest that the Ora caldera underwent main collapse along outwardly or steeply dipping faults; these are: the low lithic content of the ignimbrite succession (average 2%), limited basal breccia deposits, huge thickness of ponded ignimbrite and lack of an underlying Plinian fallout deposit (Willcock et al., 2013). Additionally, the absence of the Plinian deposit suggests an atypical eruption process, without the initial high buoyant Plinian eruption column phase, discussed further in Section 5.3. Instead this is indicative of a rapid, relatively passive collapse process at the onset of caldera eruption.

The eruption style was interpreted as being a multi-vent fissure eruption, producing relatively low intensity, continually gravitationally collapsing, hot, dense, eruption fountains feeding the pyroclastic flow system (Willcock et al., 2013). Such an eruption style has been previously interpreted to have caused restricted winnowing processes during eruption and from the top of pyroclastic flows, with the ensuing pyroclastic flow pulses thought to be hot and poorly expanded (Schmincke, 1974; Smith and Cole, 1997; Beddoe-Stephens and

Fig. 4. Groundmass and matrix crystal population shape variation (representative traced shapes only). (a) Typical phenocryst morphologies (whole and fractured) within the groundmass of juvenile clasts in the ignimbrite. (b) Typical crystal fragment morphologies in the matrix, note in situ crystal fragmentation, and (bi.–v.) representative crystal size distribution variations in the matrix of the main lithofacies (i. coarse-crystal-rich lapilli-tuff; ii. coarse-crystal-rich lapilli-tuff: bimodal crystal sub-facies; iii. vitrophyre lapilli-tuff; iv. lithic-rich lapilli tuff; v. fine-crystal-rich lapilli-tuff). Note in (v) that the fine-crystal-rich lapilli-tuff lithofacies crystals have a distinct texture, showing increased rounding, sorting and decreased total crystallinity.

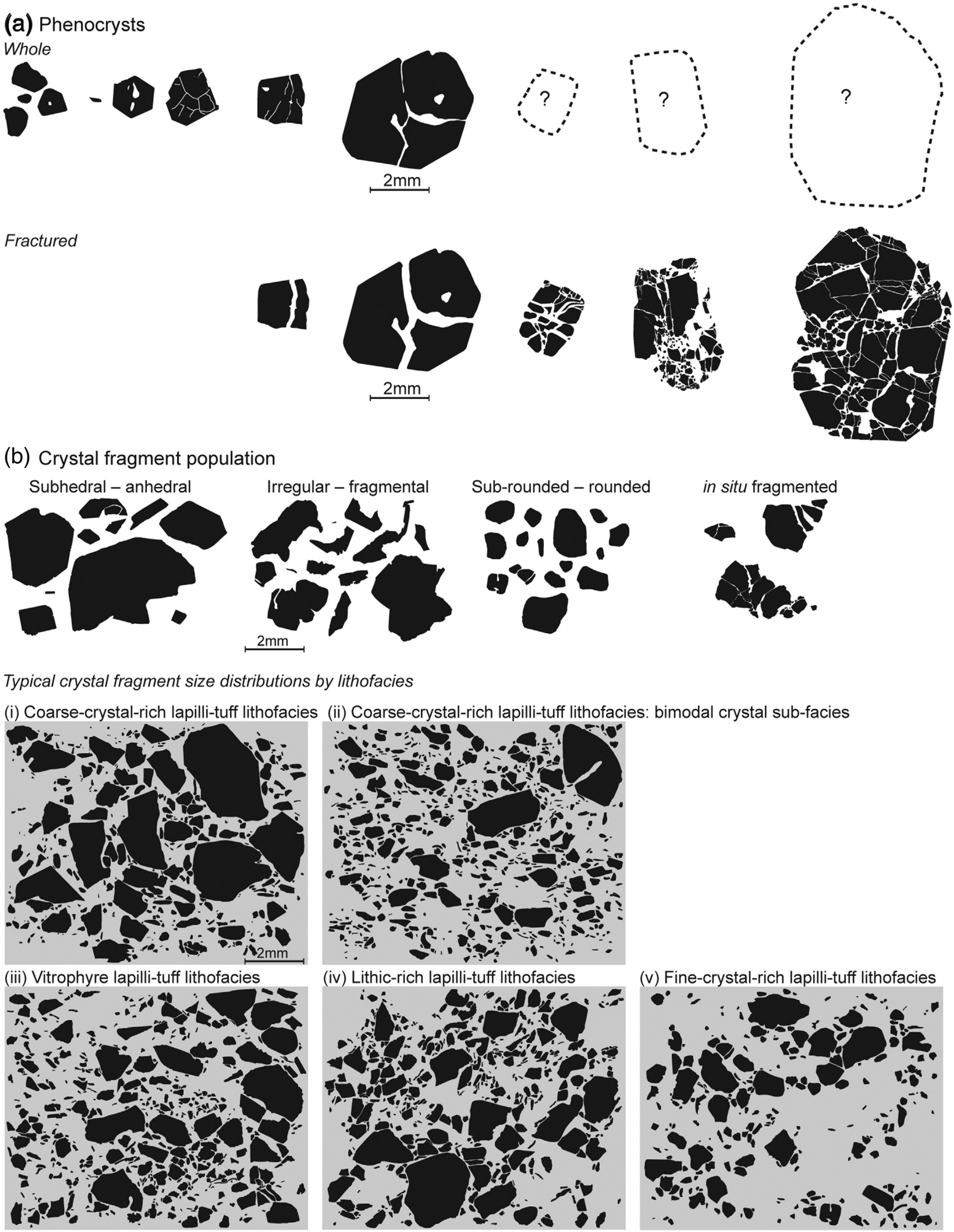
(a) Phenocrysts
Whole
?
?
?
2mm
Fractured
2mm
(b) Crystal fragment population
Subhedral – anhedral
Irregular – fragmental
Sub-rounded – rounded
in situ fragmented
2mm
Typical crystal fragment size distributions by lithofacies
(i) Coarse-crystal-rich lapilli-tuff lithofacies
(ii) Coarse-crystal-rich lapilli-tuff lithofacies: bimodal crystal sub-facies
2mm
(iii) Vitrophyre lapilli-tuff lithofacies
(iv) Lithic-rich lapilli-tuff lithofacies
(v) Fine-crystal-rich lapilli-tuff lithofacies

Millward, 2000; Lesti et al., 2011). This is supported in the Ora ignimbrite succession by low crystal concentration factors in the ash matrix relative to crystal contents in the juvenile pumice fiamme, the pervasive flow-induced grain alignment fabrics (Willcock et al., 2014), and by deposit welding (Willcock and Cas, 2014), all of which imply suppressed turbulence and laminar shear forces close to the depositional boundary (Tarling and Hrouda, 1993; Freundt, 1998; Branney and Kokelaar, 2002).

3. Materials and methods

We carried out petrographic, geochemical (X-ray Fluorescence), microprobe (Scanning Electron Microprobe-Energy Dispersive X-ray), inductively coupled plasma-mass spectrometry (ICP-MS) and cathodoluminescence (CL) analyses to better understand the intra-caldera architecture, and any vertical or lateral mineralogical or compositional deposit variations. The main geochemical sampling density was undertaken in the Northern intra-caldera, with restricted sampling in the Southern intra-caldera and northern and southern extra-caldera regions.

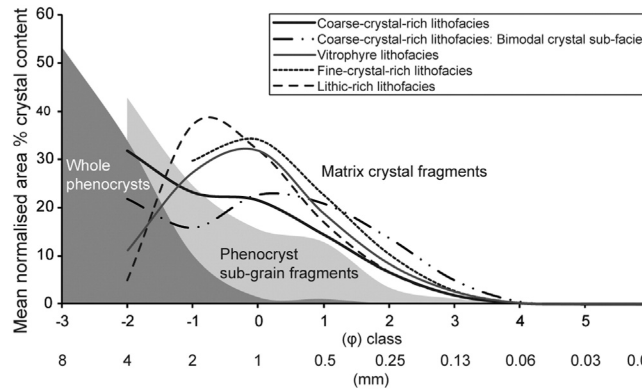

Fig. 6. Histogram of mean crystal size distributions for the Ora Formation ignimbrite lithofacies (area %), and a sample set of phenocrysts (20 whole phenocrysts and 11 fragmented phenocrysts analysed). Note the restricted size range of the fine-crystal-rich lapilli-tuff lithofacies. Sieve sizes represent lower sieve for each size grade. $\varphi = -\log2(d)$, where d is particle diameter in mm. Note that sieve sizes are computer generated.

3.1. Petrography

Petrographic descriptions, image analyses, and mineral point counting analyses were carried out at Monash University, Australia. Point counting analysis was carried out on 128 thin sections (930 counts per section, counts relate to dense rock equivalent, locations 1–14), primarily to determine abundances of the matrix and crystal fragments. Where possible point counting was also carried out on juvenile clasts, to define the type and proportion of phenocrysts and groundmass (variable counts per clast due to clast size limitations, 100 clasts counted). Outlines of phenocrysts in juvenile clasts and crystal fragments in the matrix were manually traced (from photomicrograph images 80 mm^2) using Adobe illustrator™ and then processed using ImageJ™ (Rasband, 2011), to define the crystal size distributions of phenocrysts (whole and fragmented; 20 crystals processed) and matrix crystal fragments (32 analyses across the ignimbrite lithofacies, minimum 200 crystals/analysis). These data were used for size and shape comparison of the two populations using computer generated sieve sizes. This was necessary due to the deposit welding, excluding physical sieving of samples.

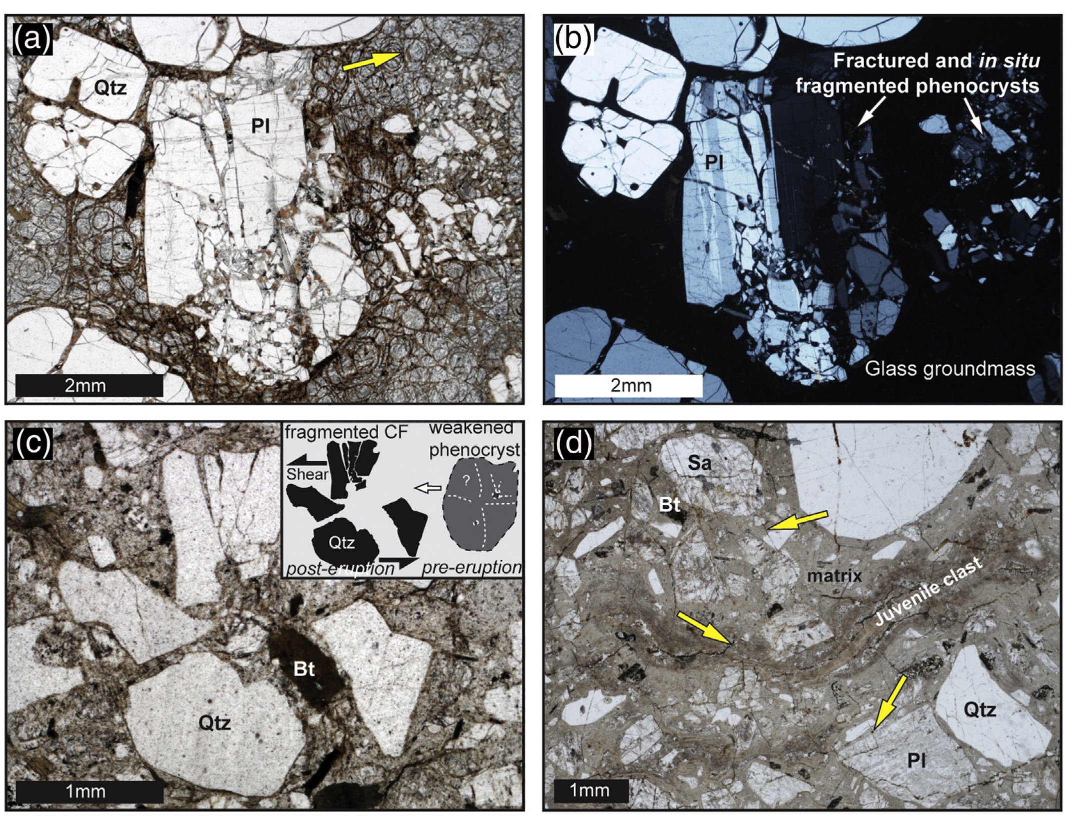

Fig. 5. Photomicrographs of the common crystal and matrix fracturing within the Ora ignimbrite succession. (a–b) PPL and XPL examples of 'phenoclast-like' plagioclase microstructure (vitrophyre lapilli-tuff lithofacies; location 4). Note perlitic fracturing in glass groundmass (PPL; see arrow), in situ crystal shattering, and jigsaw fit of phenocrysts. (c) Common quartz crystal fragment fragmentation and rotation within the matrix. Inset: possible progression from weakened quartz phenocryst to fragmented matrix crystal fragment (coarse-crystal-rich lapilli-tuff lithofacies; location 14). (d) Typical late-stage fracturing in ignimbrite matrix, note that fractures cross-cut the matrix, juvenile clasts, and crystal fragments (see arrows; coarse-crystal-rich lapilli-tuff lithofacies; location 2).

3.2. Bulk-rock X-ray fluorescence (XRF) and microprobe (SEM-EDX)

We analysed 46 ignimbrite samples for major and trace elements by X-ray fluorescence (XRF) analysis from the Southern and Northern intra-caldera successions (locations 2–3 and 14), intra-caldera ridge (location 4), and the northern caldera margin and extra-caldera ignimbrite (locations 5–7 and 12; Fig. 1c). A further nine samples were analysed for rare earth elements (REE) from the main intra-caldera successions (locations 2, 3 and 14), Northern caldera margin/extra-caldera (locations 5, 7c and 12) and Southern caldera margin/extra-caldera (location 13). These nine samples were analysed at the National Centre for Scientific Research Nancy, France. The samples were carefully selected in the field to avoid lithic contamination or strong alteration. XRF samples were milled using an agate mill, with analysis performed on pressed powder pellets. All major element data was normalised to 100%, water free, including loss of ignition (LOI), with LOI determined using gravimetry (Lamonica, 2012). The XRF precision is better than 2% for major elements and 5% for traces. The detection limits are 0.01 wt.% oxide for major elements and 2 ppm for trace elements. The probe data are greater than 2% for concentration higher than 10%, 5% in the interval 2–5 and 10% for concentration lower than 2%.

SEM-EDX microprobe analysis was carried out on minerals from 12 micro-probe slides of the Ora ignimbrite, through stratigraphic sections at locations 2, 3, 7c and 14 (Fig. 1c). The data were processed using ZAF routines provided by the analytical software (EDAX DX4). Natural minerals (silicates and oxides from the Smithsonian Microbeam Standards collection: http://mineralsciences.si.edu/faculties/standards.

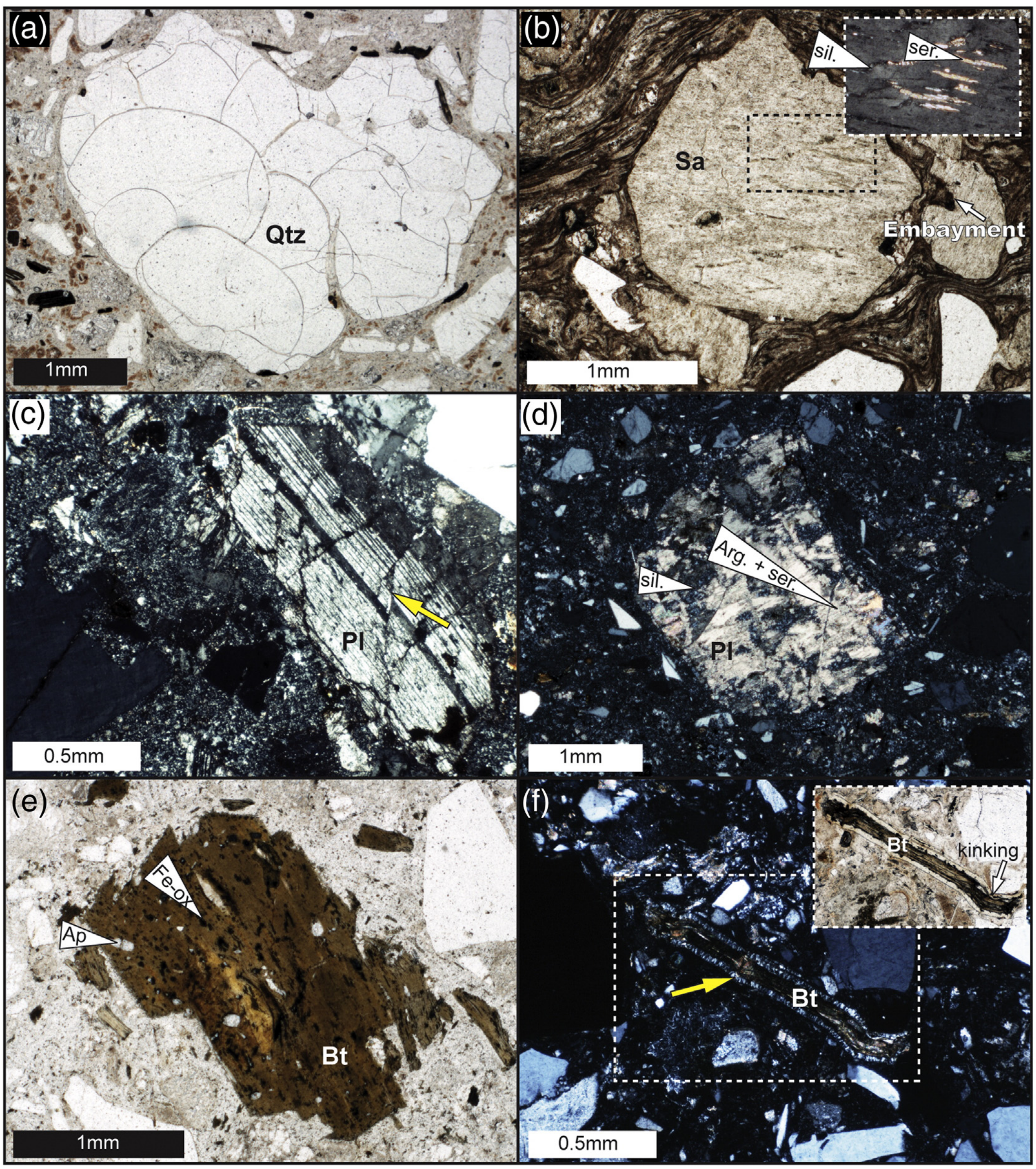

Fig. 7. Photomicrographs depicting the main mineral phases of the Ora ignimbrite succession. Volcanic quartz: (a) PPL photomicrograph of common embayments (coarse-crystal-rich lapilli-tuff: bimodal crystal sub-facies; location 4). (b) Sanidine, PPL image illustrating typical weak argyllic (arg.) + sericitic (ser.) alteration (central brown fragmented crystal; fine-crystal-rich lapilli-tuff lithofacies; location 5). Inset shows an XPL image of the sericitic and microcrystalline quartz (silicification; sil.) exsolution in-fill material. (c) Plagioclase, XPL image depicting common crystal fracturing, note the offset crystal twins (see arrow), and (d) plagioclase pseudomorph, with strong domainal alteration, mainly ser. + arg. + sil. Coarse-crystal-rich lapilli-tuff lithofacies and coarse-crystal-rich lapilli-tuff: bimodal crystal sub-facies respectively, location 2. (e) PPL image of a fragmented tabulate biotite with Fe-oxide and apatite inclusions, coarse-crystal-rich lapilli-tuff lithofacies, location 14. (f) XPL image of a kinked biotite crystal, together with axiolitic quartz and feldspar growth around the crystal margin (see arrow), coarse-crystal-rich lapilli-tuff lithofacies, location 14. Inset: PPL photomicrograph of kinked biotite crystal. (For interpretation of the references to colour in this figure legend, the reader is referred to the web version of this article.)

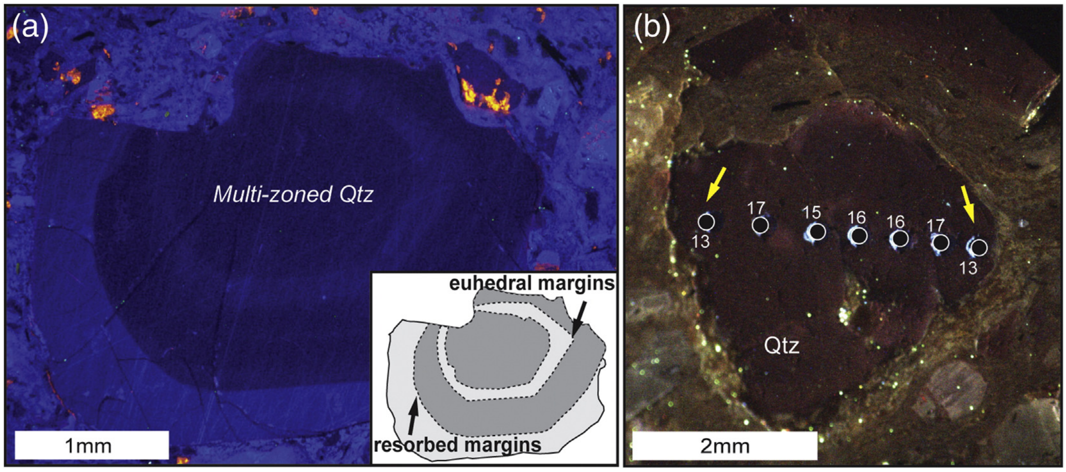

Fig. 8. (a) Cathodoluminescence (CL) image depicting oscillatory zoning within quartz. Inset: schematic drawing illustrating changes between euhedral crystal faces to irregular and round edges, recording resorption of crystal faces (coarse-crystal-rich lapilli-tuff: bimodal crystal sub-facies; location 4). The different CL bands record (b) changes from core to rim in titanium content from 18–13 (Ti ppm), showing non-uniform chemical–thermal conditions during crystal formation, fine-crystal-rich lapilli-tuff lithofacies, location 11. Note the rim-ward decrease in titanium concentration (see arrows).

htm) were used as calibration standards. The accelerating voltage was 15 kV, beam current 2 nA and counting time 100 live seconds. Data was plotted using GCDKIT (Janoušek et al., 2006). Both the XRF and the micro-probe analyses were performed at the Department of Biological, Geological and Environmental Sciences, Alma Mater Studiorum — University of Bologna, Italy.

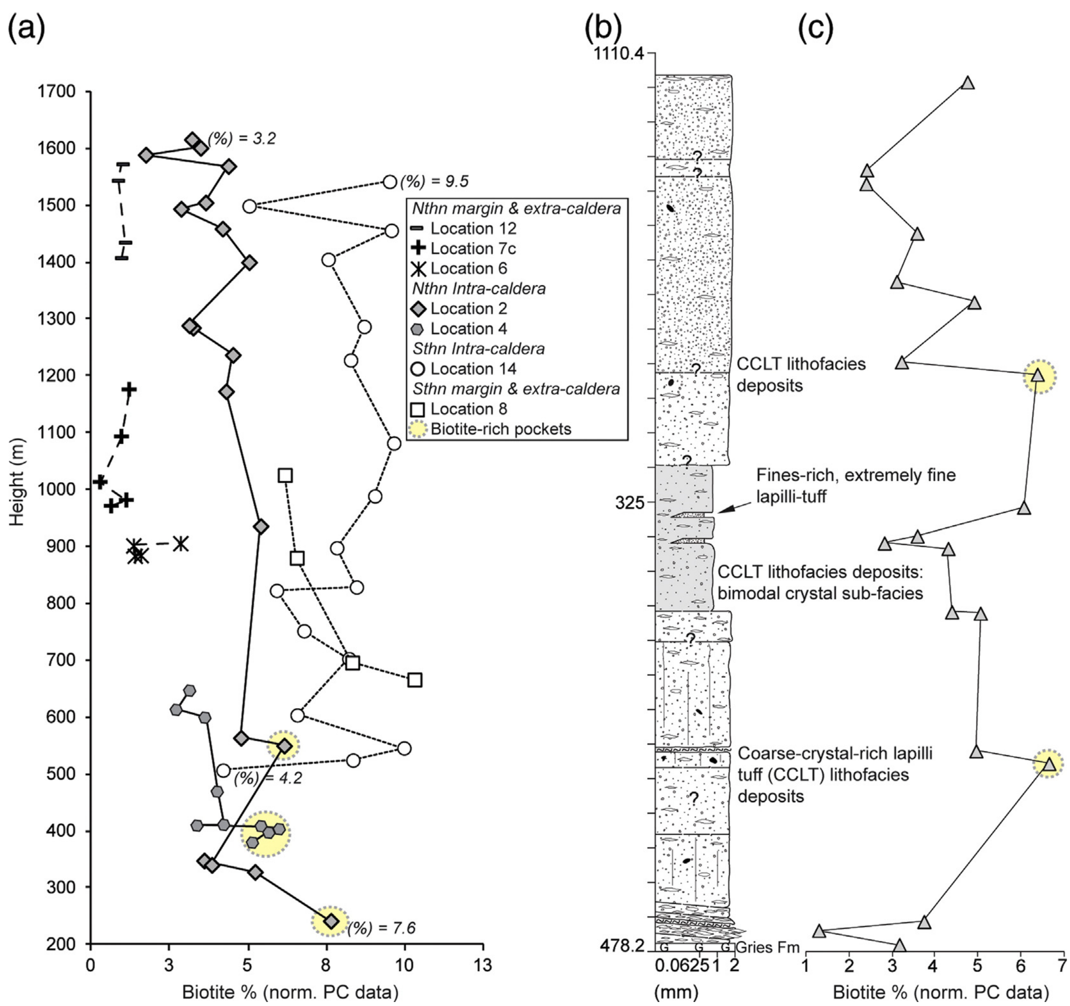

Fig. 9. Vertical ignimbrite deposit variation highlighted by changes in biotite matrix crystal fragment contents (area % point count data normalised to crystal fragments and matrix only; PC). (a) Comparison graph showing vertical deposit heterogeneity (and lateral variation) in sections taken across the caldera system from the northern extra-caldera (locations 6, 7c, 12), northern intra-caldera and caldera ridge (locations 2, 3, and 4), southern intra-caldera (location 14), and southern caldera margin/extra-caldera (location 8). Height refers to DTM height. (b–c) Biotite crystal content variation with stratigraphic height, illustrating large-scale correlation with lithofacies changes (location 3).

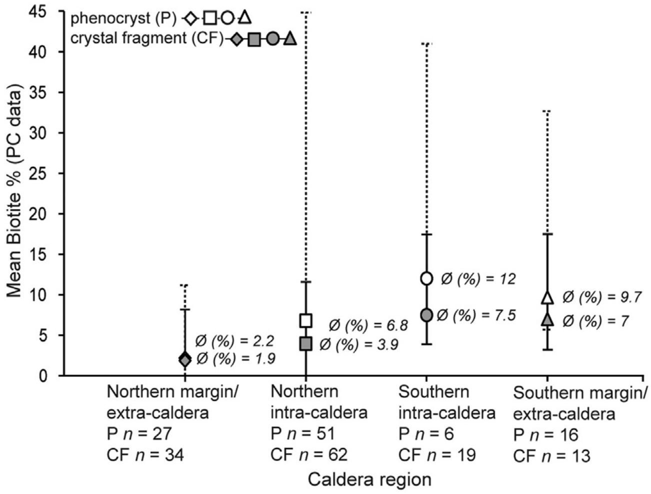

Fig. 10. Graph depicting the lateral mean biotite crystal abundance variation across the caldera system as phenocrysts in juvenile clasts (point counting carried out on phenocryst population and groundmass) and crystals within the ignimbrite matrix (normalised to crystal fragments and matrix). Note mean values between the two populations become increasingly similar northwards. Error bars represent maximum and minimum measured abundance %, note the greatest range of biotite values occurs in the Northern caldera succession.

3.3. Inductively coupled plasma-mass spectrometry (ICP-MS) and cathodoluminescence (CL) analysis

Titanium concentrations were determined by laser ablation ICP-MS, for quartz from seven ignimbrite samples from locations 2, 4, 11 and 12 (Fig. 1c). The titanium analyses were carried out using a New Wave UP 213 nm N: YAG laser ablation microprobe coupled with a Thermo Finnigan X series II, quadrupole ICP-MS, at Monash University, Australia. Analyses were performed in Helium atmosphere, analysing the following masses ^{29}Si, ^{47}Ti and ^{49}Ti, ^{43}Ca, ^{44}Ca and ^{27}Al, employing a pulse rate of 5 Hz and beam energy of ~5 J/cm^2 at the sample. Quantitative results for Ti were obtained using NIST612 glass as an external standard. Cathodoluminescence analysis (CL) was carried out on the same seven samples used for ICP-MS analysis, carried out at Melbourne University, Australia.

4. Results

4.1. Juvenile pumice clasts

Juvenile clasts are distributed throughout the Ora ignimbrite succession, with variations in clast length (<5–50 cm; generally <10 cm), shape (most commonly flattened fiamme), and phenocryst abundance (ranging from aphyric fiamme through to 'mush-like' coarsely crystalline irregular equant juvenile pumice clasts; Fig. 3). Juvenile clasts vary from still glassy (primarily observed within the vitrophyre lapilli-tuff lithofacies), to devitrified (most common), and argyllic-altered (primarily observed in the lithic-rich lapilli tuff lithofacies; Fig. 3d). Distinction of different juvenile 'types' could not be made by colour, vesicularity, alteration, or by individual compositional analysis. This was due to the large variation in colour and alteration, lack of undeformed vesicle structures, and impossibility to separate juvenile clasts from the matrix. Instead, general grouping was based on variations in phenocryst size, from very coarsely crystalline (single or multiple phenocrysts > 5 mm; Fig. 3a), coarse (3.1–5 mm; Fig. 3b–d), medium (1.1–3 mm; Fig. 3e), fine (≤1 mm; Fig. 3f), and aphyric.

All the juvenile clasts are well mixed throughout the deposit, showing no clear stratification and interestingly, many groups often occur together in the same outcrop (Fig. 3b and d–e). That said, there is a significant increase in the fine juvenile clast type within the fine-crystal-rich lapilli-tuff lithofacies, located mainly in the north-western extra-caldera setting (locations 5, 6 and 11; Figs. 1c and 3f). Within this lithofacies, the juvenile clast population is typically comprised of small-sized clasts (generally <3 cm) with small phenocrysts (generally <1 mm), showing subtle distinction from the other ignimbrite lithofacies juvenile clast populations.

4.2. Crystal populations

Ignimbrite samples reveal variably fragmented crystals within the matrix (Fig. 2b, d and f). The ignimbrite matrix mineral assemblage is largely consistent, dominated by volcanic quartz + sanidine + plagioclase + biotite, with accessory Fe-oxides (magnetite ± ilmenite), and apatite. This low degree of internal componentry variation is consistent with large caldera systems (Francis et al., 1989). Despite similar componentry, some variation in abundances of individual mineral phases is observed. Biotite is the least abundant mineral of the main population. Its abundance, however, varies between samples, enabling important large-scale discrimination within the system (Fig. 2), also shown in previous caldera studies in the Andes (de Silva and Francis, 1989; Folkes et al., 2011a).

4.2.1. Phenocryst population in juvenile clasts

Phenocrysts within juvenile clasts range in size from <1 mm to >3 cm. In general, they are <2 mm. They can be preserved as whole grains, or can be internally fractured forming sub-grains (Fig. 4a). Quartz phenocrysts are typically euhedral to subhedral with common resorption embayments and occur up to ~2 cm in size. Sanidine phenocrysts are more commonly subhedral, subtly to moderately altered (following the scheme of Gifkins et al., 2005), with widespread in situ fragmented crystals, up to ~3 cm in size (Fig. 4a). Plagioclase is comparable in size to sanidine, euhedral to subhedral, subtly to strongly altered, and typically fractured with common fragmented crystal morphologies. Biotite is also generally euhedral to subhedral, unaltered to strongly altered, and is noticeably smaller than the other phenocrysts, reaching up to 3 mm. Fractured phenocrysts display weak to extreme in situ fragmentation, with some showing similarity to 'phenoclast'

Table 2
Mean point-count ignimbrite crystal population abundance variations by caldera region (area %).

	Southern intra-caldera CF: $n = 6$ P: $n = 19$	Southern margin/extra-caldera $n = 16$ $n = 13$	Northern intra-caldera $n = 51$ $n = 62$	Northern margin/extra-caldera $n = 27$ $n = 34$
Phenocryst (P)				
Biotite	12 ± 8.8[a]	9.7 ± 4.7	6.8 ± 6.8	2.2 ± 1.8
Plagioclase	9.2 ± 8	3 ± 1	5.2 ± 5.3	2.8 ± 2.2
Crystal fragments (CF)				
Biotite	7.5 ± 1.9	7 ± 1.9	3.9 ± 1.4	1.9 ± 1.7
Plagioclase	18.3 ± 4.2	12.7 ± 4.8	5.4 ± 6.3	6.3 ± 3.3
Total crystal fragments	61.5 ± 3.8	61 ± 5.6	54.8 ± 8.9	49.9 ± 5.3

[a] One standard deviation as a %, n = number of samples counted. Data normalised to the total area minus juvenile and lithic-clasts.

phenocryst aggregates (Best and Christiansen, 1997; Fig. 5a–b). Fracturing and fragmentation of the phenocrysts commonly results in a jigsaw fit texture (Fig. 5a–c).

4.2.2. Matrix crystal fragment population

Crystal fragments range from <0.06 mm to ~1 cm (commonly 1–2 mm; Figs. 4b–6). Variations in size across the ignimbrite lithofacies are subtle, but were pivotal in enabling lithofacies division (Fig. 4bi–v). They are also commonly fractured and display crystal rotation within the matrix (Fig. 5c–d), together with some in situ crystal fragmentation (Fig. 4b).

Quartz crystal fragments are commonly resorbed (Fig. 7a). They are typically subhedral to fragmental, with sub-rounded (especially common within the fine-crystal-rich lapilli-tuff lithofacies) and lesser blocky and sliver shapes (Fig. 4b), clear, and show some zonation, identified by cathodoluminescence (CL) analysis (Fig. 8a). The zoned crystals display alternating zones of variable widths, with an oscillatory pattern, reflecting variation in titanium concentration during crystal growth (Fig. 8b). CL zones vary in shape from straight edged, defining internal euhedral crystal faces, to rounded and minor irregular margins (Fig. 8a), indicative of resorption occurring at the end of the specific growth event (Ruffini et al., 2002).

Feldspar crystal fragments are typically altered (Fig. 7b–d), generally subhedral to anhedral, with tabulate to fewer blocky to sub-rounded shapes, unzoned (rare oscillatory zoning observed in the vitrophyre lapilli-tuff lithofacies), and fractured. Sanidine crystal fragments are clear to pale brown in colour (Fig. 7b), and typically subtly to moderately altered, dominated by argyllic alteration (clay mineral replacement), showing early mineral bleaching, together with common sericitic alteration + oxidation + silicification. Due to the common low degree of alteration and lack of twinning, we have used their straight cleavage networks, to distinguish them from quartz. Plagioclase crystal fragments are generally cloudy to pale brown in colour, chiefly andesine ≈ $An_{35–25}$, and moderately to strongly altered. The main alteration phases include argyllic + sericitic + calcite + oxidation + silicification, with alteration commonly to such an extent that identification is difficult.

Biotite crystal fragments range from euhedral to anhedral, and display tabulate, blocky, hexagonal and irregular shapes, with examples of kinked crystals found (Fig. 7e–f). Biotite typically defines a foliation in thin section and commonly has mineral inclusions, primarily small Ap + Mag + Ep + Ilm + Mnz (Fig. 7e; abbreviations after Kretz, 1983). Biotite crystals are generally relatively fresh, yet are also shown to be strongly altered, with complete oxidation, or showing local chloritization (common in the basal intra-caldera setting) and rare sericitic alteration. Additionally, sporadic occurrences of axiolitic quartz and feldspar growth around the margins of some biotite crystals is noted (Fig. 7f).

Table 3
Regional bulk-rock composition of major (wt.%) and trace elements (ppm) for the Ora Formation ignimbrite succession.

	SiO_2 (wt.%)	TiO_2 (wt.%)	Al_2O_3 (wt.%)	Fe_2O_3 (wt.%)	MnO (wt.%)	MgO (wt.%)	CaO (wt.%)	Na_2O (wt.%)	K_2O (wt.%)	P_2O_5 (wt.%)	LOI
Southern intra-caldera (n = 10)											
Mean	74.12	0.29	13.60	2.35	0.08	0.78	0.60	3.51	4.59	0.07	1.51
Median	74.28	0.29	13.47	2.35	0.08	0.78	0.51	3.50	4.55	0.07	1.17
St. dev	0.62	0.02	0.41	0.10	0.01	0.13	0.38	0.37	0.23	0.01	0.88
Min.	73.01	0.27	13.10	2.18	0.07	0.54	0.26	2.87	4.34	0.07	0.74
Max.	74.79	0.34	14.44	2.57	0.09	1.02	1.54	4.07	5.17	0.08	3.64
Northern intra-caldera (n = 27)											
Mean	74.84	0.23	14.06	1.65	0.07	0.38	0.69	2.14	5.90	0.04	1.82
Median	74.79	0.26	13.90	1.56	0.07	0.33	0.38	2.42	5.97	0.05	1.69
St. dev	1.31	0.07	0.97	0.47	0.01	0.16	0.65	0.94	0.78	0.02	0.83
Min.	72.49	0.10	12.70	0.78	0.05	0.21	0.09	0.51	3.56	0.00	0.32
Max.	76.88	0.33	15.89	2.56	0.10	0.73	2.35	3.54	7.10	0.09	3.61
Northern extra-caldera (n = 9)											
Mean	76.73	0.10	13.35	1.41	0.06	0.25	0.38	1.99	5.71	0.01	1.50
Median	76.61	0.10	13.58	1.37	0.06	0.22	0.32	2.09	5.57	0.01	1.50
St. dev	0.57	0.01	0.64	0.15	0.01	0.10	0.26	0.98	0.60	0.01	0.38
Min.	76.01	0.08	12.30	1.23	0.05	0.17	0.10	0.52	4.97	0.00	0.88
Max.	77.73	0.11	14.29	1.68	0.07	0.48	0.95	3.49	6.53	0.03	2.15

	Sc (ppm)	V (ppm)	Cr (ppm)	Co (ppm)	Ni (ppm)	Zn (ppm)	Rb (ppm)	Sr (ppm)	Y (ppm)	Zr (ppm)	Nb (ppm)	Ba (ppm)	La (ppm)	Ce (ppm)	Pb (ppm)	Th (ppm)
Southern intra-caldera (n = 10)																
Mean	5.2	20.40	6.67	4.43	4.78	44.70	224.10	91.40	34.90	193.90	12.30	322.70	26.80	57.00	25.00	21.80
Median	5	20.00	6.00	4.00	5.00	49.00	219.50	91.00	34.00	193.00	12.50	318.50	27	56	25.50	22
St. dev	1.23	2.17	1.94	0.53	0.83	11.74	20.38	24.81	3.38	11.88	1.34	34.69	8.19	9.13	4.74	2.15
Min.	4	17	4	4	4	24	199	56	32	178	10	279	13	41	15	19
Max.	7	25	11	5	6	59	262	135	41	218	14	407	39	67	30	26
Northern intra-caldera (n = 27)																
Mean	5.7	13.83	5.80	4.00	4.08	35.00	259.96	59.23	46.11	194.48	12.48	413.22	36.85	74.15	24.48	20.15
Median	6	15.00	5.00	4.00	4.00	29.00	255.00	45.50	40.00	216.00	12.00	406.00	38	75	22	20
St. dev	2.27	4.43	2.05	0.00	0.28	16.52	52.37	40.13	15.49	49.77	1.67	220.42	10.20	18.79	7.55	2.20
Min.	2	5	4	4	4	14	176	14	28	98	10	154	14	36	12	14
Max.	10	22	8	4	5	78	368	184	79	266	17	1151	53	105	49	23
Northern extra-caldera (n = 9)																
Mean	4.22	ND	ND	ND	4.50	32.44	283.78	23.80	53.78	110.33	14.11	102.11	23.33	51.9	23.6	21
Median	5	ND	ND	ND	4.50	25.00	255.00	17.00	53.00	110.00	15.00	98.00	24	55	23	22
St. dev	1.72	ND	ND	ND	0.58	17.69	65.85	16.04	12.96	16.37	1.96	20.91	5.66	9.64	3.88	3.162
Min.	1	ND	ND	ND	4	16	216	11	30	88	11	80	13	32	18	16
Max.	6	ND	ND	ND	5	69	383	51	70	130	17	147	30	64	29	25

* Major elements normalised to 100%, st. dev. = Standard deviation, LOI = loss on ignition.

Table 4
Selected bulk-rock trace element concentrations (ppm) and TiO_2 (wt.%) by region for the Ora Formation ignimbrite succession.

	Hf (ppm)	Nb (ppm)	Ta (ppm)	Th (ppm)	U (ppm)	Y (ppm)	Zr (ppm)	TiO_2 (wt.%)
Southern caldera (n = 2)								
Location 14 (lower)	4.3	10.9	1.6	19.7	3.8	24.9	149.9	0.2
Location 14 (upper)	4.7	11.8	1.4	17.9	4.1	24.3	180.2	0.3
Southern caldera margin/extra-caldera (n = 1)								
Location 13 (upper)	5.3	12.2	1.2	18.2	3.3	20.7	198.8	0.4
Northern caldera (n = 3)								
Location 2 (lower)	4.1	11.1	1.2	17.8	3.9	30.6	135.7	0.2
Location 2 (upper)	5.0	10.9	1.1	21.1	3.9	26.0	186.9	0.2
Location 3 (upper)	5.5	10.6	0.9	19.8	2.1	20.0	208.3	0.3
Northern caldera margin/extra-caldera (n = 3)								
Location 5 (middle)	2.6	12.9	2.2	13.1	2.6	44.9	67.0	0.1
Location 7C (upper)	3.9	11.6	1.5	20.5	1.6	34.2	101.0	0.1
Location 12 (lower)	3.6	14.4	1.8	23.9	2.4	39.5	87.0	0.1

4.3. Image analysis of the crystal populations

Image analysis on photomicrographs reveals that whole phenocrysts mostly fall within the 8–2 mm range (−3 to −1φ grade). In contrast, measured internal phenocryst sub-grains generally fall within the 4–0.25 mm range (−2 to 2φ), with high modes at 4 and 0.5 mm (−2 and 1φ; Fig. 6). Importantly, the size distribution and shape of the phenocryst sub-grains are generally comparable to the crystal fragment size distributions and shapes in the matrix (Figs. 4 and 6).

Image analysis shows that the crystal fragment population has a large size distribution from 4–0.02 mm (−2 to 6φ; Fig. 6). Fig. 6 illustrates these subtle size variations across the four ignimbrite lithofacies. The coarse-crystal-rich lapilli-tuff lithofacies has the coarsest crystal population, with a greater area percentage of crystals within the 4 mm size range (−2φ; CCLT). The coarse-crystal-rich lapilli-tuff bimodal sub-facies is distinct, with two strong modes at 4 and 1 mm size ranges (−2 and 0φ; CCLT: bimodal crystal sub-facies). The vitrophyre lapilli-tuff and lithic-rich lapilli tuff ignimbrite lithofacies display slightly finer crystal populations, concentrated around the 2 and 1 mm size range (−1 to 0φ; VLT and LRLT). There is a significant difference in the fine-crystal-rich lapilli-tuff ignimbrite lithofacies, which has a restricted crystal size distribution between 2 to 0.6 mm (−1 to 4φ; FCLT; Fig. 6).

4.4. Point count data: vertical and lateral variations in modality

The crystal fragment proportions of the ignimbrite succession is high (average 42.5% ± 8.3%; one standard deviation, data including total area: crystals, matrix, juvenile clasts and lithic clasts), with a range from ~25%–57%. Moreover, there was shown to be an average decease northwards in samples across the caldera system from 47–37%.

To define the average matrix mineral phase abundances we then normalised the data to the total area minus that covered by juvenile and lithic-clasts. This gave an average of 55% crystal fragments to 45% matrix, with average mineral proportions at 24% quartz (range 5–40%), 16% (3–30%) sanidine, 11% (1.5–25%) plagioclase, and 4% (<1–10.5%) biotite. Relative abundance of the main mineral phases in the matrix remain consistent across the system Qtz > Sa > Pl > Bt.

Phenocryst proportions measured from 100 juvenile clasts are moderate, with an average 26% ± 11.4% (one standard deviation), and range from ~0%–58%. Counting the area of individual phenocrysts to matrix, the mean abundance of the main phenocryst phases are: 10% quartz, 6.5% sanidine, 6% biotite, and 3.6% plagioclase. These data show a change in relative abundance between biotite and plagioclase from phenocrysts to crystal fragments. This is suggested to represent some loss of biotite in the matrix during eruption, likely reflecting the different mechanical

Table 5
Regional bulk-rock rare earth element and Y concentrations (ppm) for the Ora Formation ignimbrite succession.

	La (ppm)	Ce (ppm)	Pr (ppm)	Nd (ppm)	Sm (ppm)	Eu (ppm)	Gd (ppm)	Tb (ppm)	Dy (ppm)	Ho (ppm)	Er (ppm)	Tm (ppm)	Yb (ppm)	Lu (ppm)	Y (ppm)
Southern caldera (n = 2)															
Location 14 (lower)	21.2	60.7	4.5	17.5	3.9	0.4	3.7	0.6	3.9	0.8	2.4	0.4	2.7	0.4	24.9
Location 14 (upper)	30.8	64.4	6.4	24.9	5.0	0.7	4.4	0.7	4.2	0.8	2.2	0.4	2.4	0.4	24.3
Southern caldera margin/extra-caldera (n = 1)															
Location 13 (upper)	37.1	94.3	7.9	27.3	5.2	0.9	4.3	0.7	3.9	0.7	2.1	0.3	2.1	0.3	20.7
Northern caldera (n = 3)															
Location 2 (lower)	35.5	72.0	7.5	28.1	5.5	0.3	4.9	0.8	5.1	1.0	2.9	0.5	3.1	0.5	30.6
Location 2 (upper)	48.2	92.2	9.5	35.7	6.5	0.6	5.3	0.8	4.5	0.9	2.4	0.4	2.4	0.4	26.0
Location 3 (upper)	42.7	80.2	7.5	27.0	4.4	0.5	3.6	0.5	3.3	0.7	2.0	0.3	2.1	0.3	20.0
Northern caldera margin/extra-caldera (n = 3)															
Location 5 (middle)[a]	15.6	35.0	4.1	16.3	4.8	0.1	5.2	1.1	7.1	1.4	4.2	0.7	4.5	0.7	44.9
Location 7C (upper)	29.6	61.5	7.3	29.9	6.6	0.2	5.7	0.9	5.8	1.2	3.2	0.5	3.3	0.5	34.2
Location 12 (lower)	24.5	51.7	7.0	29.5	7.4	0.2	6.6	1.1	6.6	1.3	3.6	0.6	3.9	0.6	39.5

[a] Fine-crystal-rich lapilli-tuff lithofacies sample.

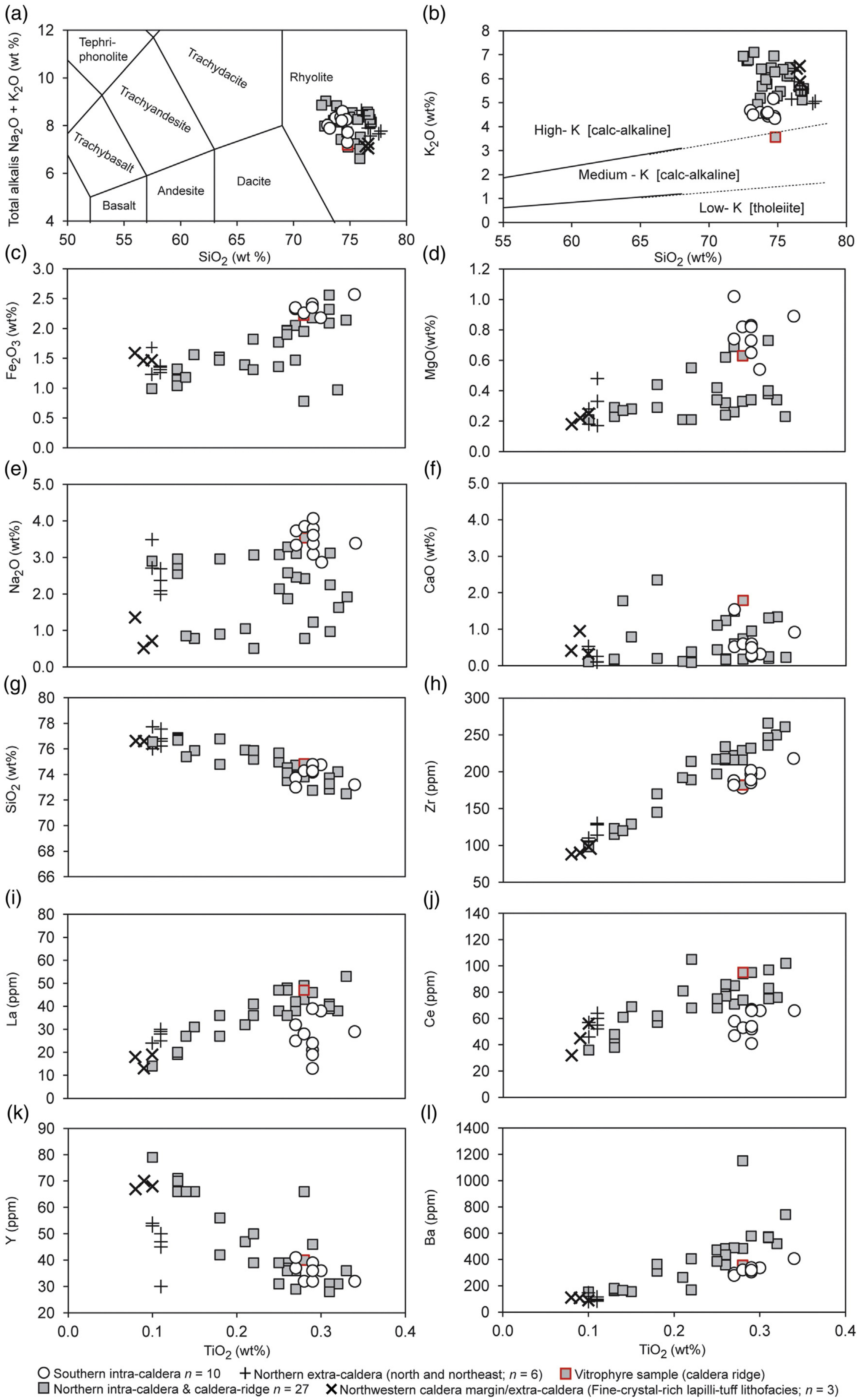

(a)
Total alkalis Na2O + K2O (wt %)
SiO2 (wt %)
Tephri-phonolite
Trachydacite
Rhyolite
Trachyandesite
Trachybasalt
Basalt
Andesite
Dacite
(b)
K2O (wt%)
SiO2 (wt%)
High- K [calc-alkaline]
Medium - K [calc-alkaline]
Low- K [tholeiite]
(c)
Fe2O3 (wt%)
(d)
MgO(wt%)
(e)
Na2O (wt%)
(f)
CaO (wt%)
(g)
SiO2 (wt%)
(h)
Zr (ppm)
(i)
La (ppm)
(j)
Ce (ppm)
(k)
Y (ppm)
(l)
Ba (ppm)
TiO2 (wt%)
Southern intra-caldera n = 10
Northern extra-caldera (north and northeast; n = 6)
Vitrophyre sample (caldera ridge)
Northern intra-caldera & caldera-ridge n = 27
Northwestern caldera margin/extra-caldera (Fine-crystal-rich lapilli-tuff lithofacies; n = 3)

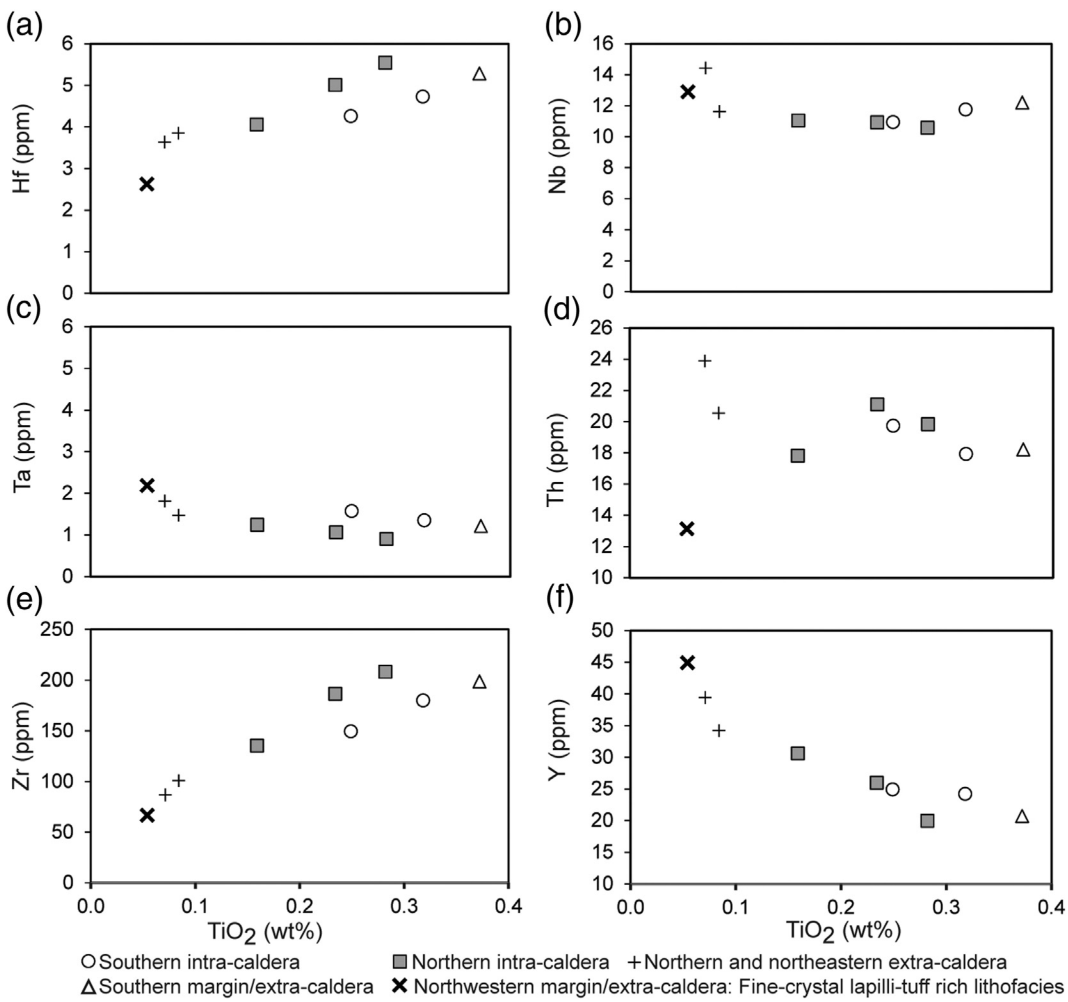

Fig. 12. Selected high field strength element (HFSE), plotted against TiO_2. Note the clear separation of the southern (intra and extra) succession, northern intra-caldera succession and northern extra-caldera succession highlighted particularly in (a), (c), (e) and (f). Moreover, the separation of the fine-crystal-rich lapilli-tuff sample in (a), (d)–(f).

strengths of the minerals and related breakage during eruption, as well as differences in the hydrodynamic behaviour in the eruption column. Alternatively, it may reflect original variations in biotite abundance in the magma(s).

We present point count data from individual stratigraphic sections to illustrate any base to top and large-scale lateral variation across the whole deposit (Fig. 9). We also group results by caldera region: Southern and Northern intra-caldera and southern and northern extra-caldera (Fig. 10; Table 2). Particular emphasis was placed on abundance variations of biotite. We also present plagioclase and total crystal fragment abundances, to better understand the overall mineralogical architecture of the succession (Table 2).

Biotite crystal fragment abundance varies through vertical sections in the intra-caldera succession (e.g. location 2 ranges from 1.7–7.6%; Fig. 9a; data normalised to the total area minus juvenile and lithic-clasts). Comparison of biotite variation across individual stratigraphic sections also shows differences in abundance. The Southern intra- and extra-caldera sections generally display higher biotite abundances (e.g. locations 14 and 8), than the Northern caldera sections (e.g. locations 2 and 4; Fig. 9a). Moreover, the deposits located in the northern extra-caldera have the lowest biotite abundances (e.g. locations 6, 7c, and 12), reflecting a large-scale northwards decrease in biotite crystal fragments (Figs. 1c and 9a). Additionally, when the data are compared to the parent stratigraphic sections, there is some local correlation between crystal fragment biotite variations and lithofacies changes (e.g. location 3; Fig. 9b). In summary, the Northern succession samples are shown to have a reduced content of biotite crystal fragments and phenocrysts and wider variance, when compared to the Southern samples (Fig. 10; Table 2).

4.5. Bulk-rock chemistry

Our data albeit limited show some important major and trace element changes between the main ignimbrite deposits of the Ora system. Sampling was undertaken throughout representative stratigraphic sections, divided into; the Southern intra-caldera (location 14) and caldera margin/extra-caldera (location 13; only for REE data), intra-caldera ridge (location 4), Northern intra-caldera (locations 2 and 3), and caldera margin/extra-caldera (locations 5, 6, 7c, and 12; Fig. 1c; Tables 3–5).

Fig. 11. Selected bulk-rock major and trace element variation diagrams, plotted against SiO_2 (a–b) and TiO_2 (c–l). Analyses (a–g) are normalised to 100% volatile free. The ignimbrite has a rhyolitic composition on the TAS diagram (a), and a medium to high-K character (b), after the IUGS classification of Le Maitre et al. (1989). Note the ranges of major and trace element values (d–l), together with the lateral differences between the Southern and Northern succession samples.

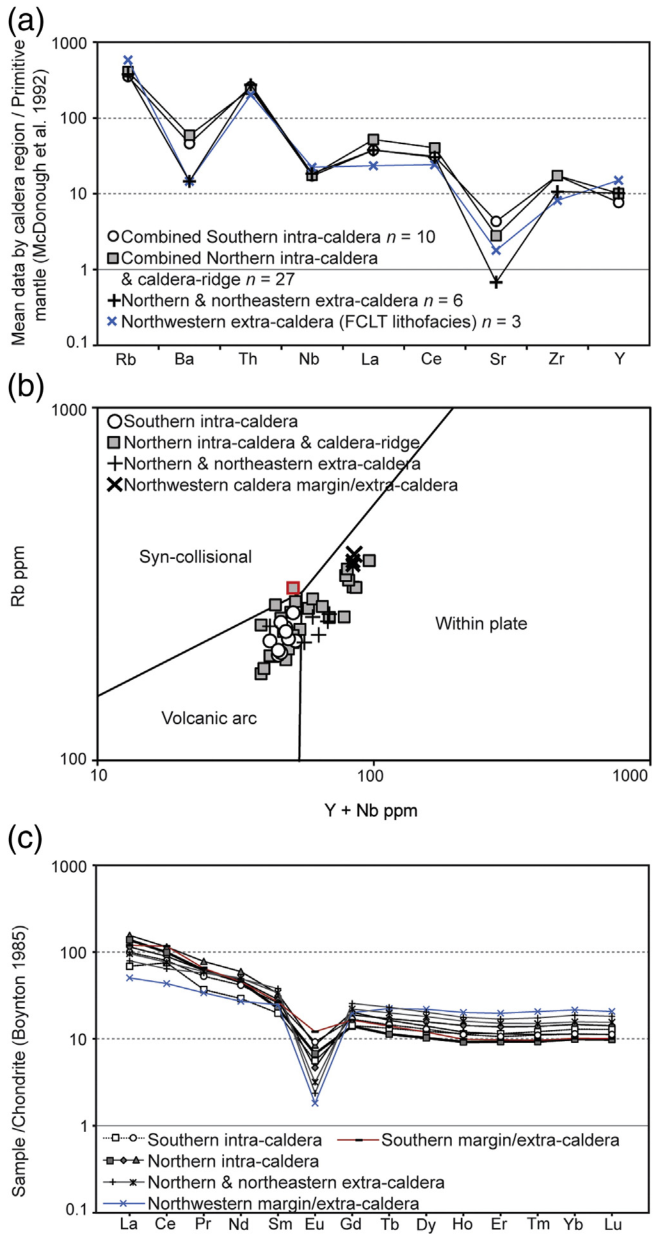

Fig. 13. (a) Multi-element patterns, normalised to Primitive mantle after McDonough et al (1992); (b) granite discrimination diagram (Y + Nb vs. Rb) after Pearce et al. (1984); and (c) rare earth element (REE) patterns normalised by Chondrite after Boynton (1985), for the Ora Formation ignimbrite succession. Note in (a) the distinct values of the extra-caldera samples for Ba, Sr and Zr and in (b) the different values of samples for different regions for Eu and HREE elements and the similarity of the southern extra-caldera and northern intra-caldera samples.

Analysis was undertaken to further explore the broad lateral and base-to-top deposit variation highlighted by the mineralogical data.

The following points were considered when undertaking field sampling and the chemical analysis of these rocks:

(1) The region underwent hydrothermal alteration (primarily Triassic) with possible mobilization of major and trace elements, e.g. K_2O, Na_2O, Rb, Sr and Ba and high LOI (D'Amico and Del Moro, 1988; Barth et al., 1993; Rottura et al., 1998b). To counter this we considered also immobile trace and rare earth element (REE) and single mineral data (Figs. 11–15; Tables 3–5);

(2) Ignimbrite composition may be influenced by physical fractionation processes, such as fines winnowing and crystal enrichment. These processes can significantly alter the geochemical signature of the deposit from the primary magma, discussed in Section 5.1.2 (Walker, 1972; Sparks and Walker, 1977).

(3) Contamination by xenolithic and xenocrystic material may result in compositional heterogeneity in a deposit from a homogeneous source magma, e.g. the Fish Canyon Tuff (Whitney and Stormer, 1986), or extreme values for the main mineral phases (Beddoe-Stephens and Millward, 2000). We selected samples for analysis with low lithic clast contents (<2%), minimizing scattering due to lithic clast content. The similarity in mineralogy of the main ignimbrites of the Athesian Volcanic Group meant no clear distinction could be made between crystals originating as phenocrysts from the Ora eruption and possible xenocrysts from earlier eruptive events.

4.5.1. Major and trace elements

The combined data presented in Table 3 reveals a relatively restricted SiO_2 range between 72.5–77.7% (average 74%–76.7%) for the ignimbrite (Table 3). The ignimbrite samples all plot within the rhyolite field on the total alkali versus silica (TAS) diagram (Fig. 11a; Le Bas et al., 1986; Le Maitre et al., 2002). Interestingly, Fig. 11a shows a separation between the Southern intra-caldera and northern extra-caldera samples, with the Northern intra-caldera samples overlapping the two. The ignimbrite as a whole is calc-alkaline and high-K (Fig. 11b; see also Barth et al., 1993; Marocchi et al., 2008). Only the slightly hydrated vitrophyre sample plots as medium-K (Le Maitre et al., 1989). The selected major and trace element variation diagrams illustrate positive trends for Fe_2O_3, MgO, La, Ce, Zr, Hf and Ba, negative trends for SiO_2, Ta, Nb and Y, and scattered results for Na_2O, CaO, and Th, with TiO_2 (Figs. 11b–l and 12; Tables 3–4). The vitrophyre sample is shown to have anomalously low K_2O, moderate CaO, and MgO, and high Na_2O, Fe_2O_3, La, and Ce (red square; Fig. 11). In general, large element variations are noted for Fe_2O_3 (0.78–2.57%), MgO (0.17–1.02%), TiO_2 (0.08–0.34%), and trace elements Zr (88–266), Rb (176–383), Ba (80–1151), and Sr (11–184; Fig. 11c–l). The higher loss on ignition for samples from the Northern intra-caldera succession could indicate greater alteration, or the influence of a few anomalous outlier samples (Table 3).

The multi-element patterns for the ignimbrite, normalised to primitive mantle (after McDonough et al., 1992), all show a similar pattern, reflecting a genetic relationship across the ignimbrite (Fig. 13a; Table 5). That said, the north-western margin/extra-caldera fine-crystal-rich lapilli tuff lithofacies does show higher Rb, Nb and Y values. The patterns show general incompatible element enrichment and compatible element depletion compared to the primitive mantle. This is illustrated by the general negative slope of the plot; enrichment of Rb, the light rare earth elements (LREE) of La and Ce, and high field strength (HFS) element Th; and depletion of Ba, Sr and the HFS elements of Zr and Y (Fig. 13a). The low Nb value could relate to previous subduction and mantle/crustal mixing-related signatures during formation of the long lived Athesian Volcanic Group system. While the depletions in Ba and Sr likely reflect element mobility due to post-emplacement alteration, as illustrated by the large element ranges (Fig. 11l and Tables 3–5). These data are consistent with previous works, which suggest such trends reflect previous subduction and mantle and crustal contributions (Barth et al., 1993; Timmerman, 2004). A complex tectonic and magmatic history is further supported by the Rb vs. Y + Nb discrimination plot (after Pearce et al., 1984), with samples sitting across the volcanic arc, syn-collisional and within-plate granite fields, indicating a change in tectonic setting during magma evolution (Fig. 13b).

The rare earth element patterns, normalised to chondrite (after Boynton, 1985) show that the heavy rare earth elements (HREE) are incompatible, while the LREE are compatible in the system (Fig. 13c; Table 5). The LREE patterns may reflect fractionation of apatite and monazite accessory phases from less evolved parental magma(s). There is a strong negative Eu anomaly, likely a result of the removal of feldspar from the parental magma(s) in the crust (e.g. Barth et al., 1993). The greatest difference is noted in the magnitude of Eu depletion,

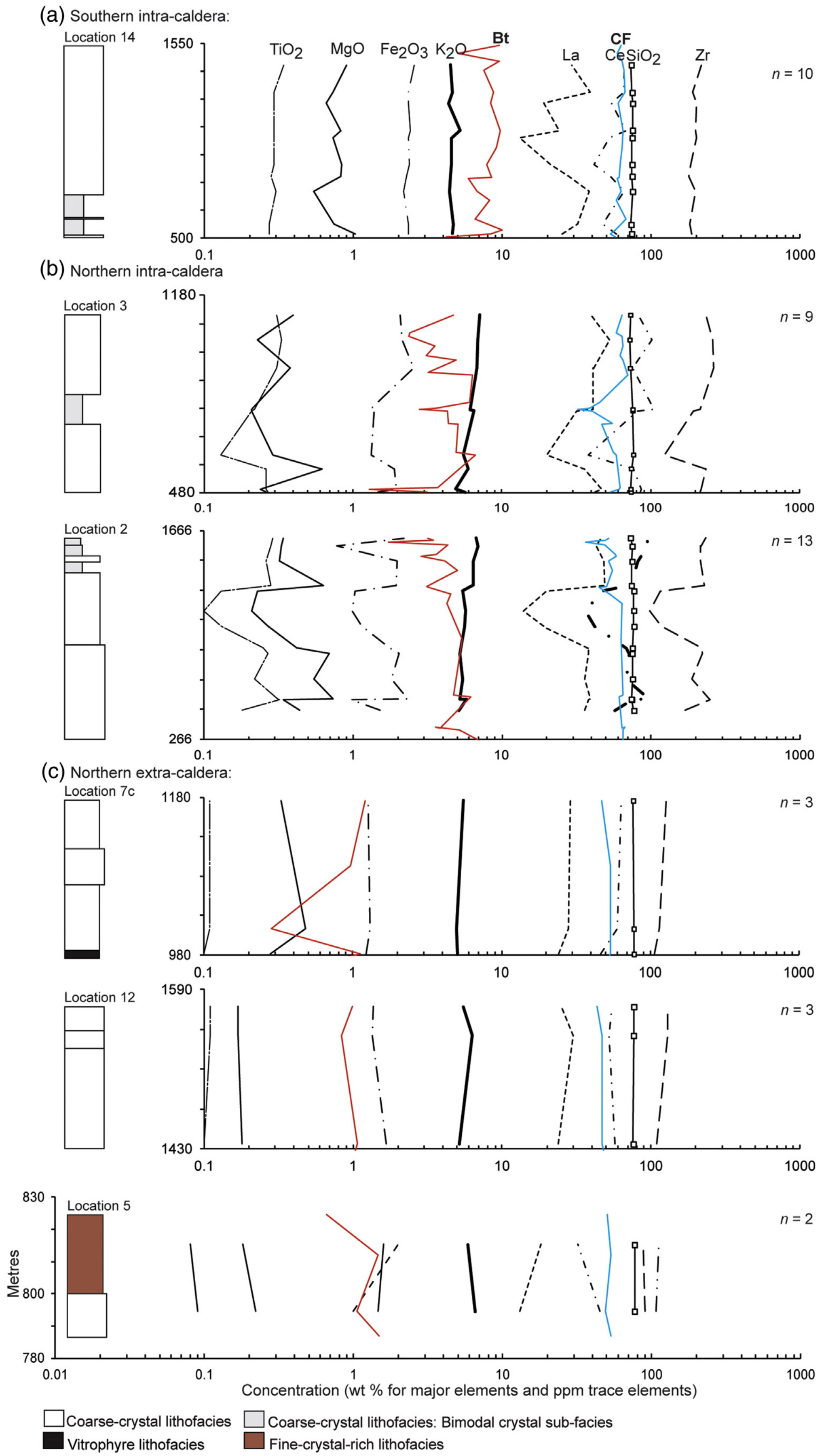

Fig. 14. Representative vertical variation of chemical, biotite (Bt) crystal fragment, and total crystal fragment data (CF). (a) Southern caldera (location 14), (b–c) intra-caldera ridge and northern intra-caldera (locations 2, 3, and 4), and (d) the northern extra-caldera (locations 5 (northwest), 7c (northeast), and 12 (north)). Note the absence of uniform vertical zonation between stratigraphic sections and chemical heterogeneity and local zonation within individual stratigraphic sections. *n* refers to number of geochemical samples, log scale used to demonstrate the large spread of data. The schematic sections to the left of the graphs demonstrate a relative association of the vertical chemical changes with large-scale variation in lithofacies.

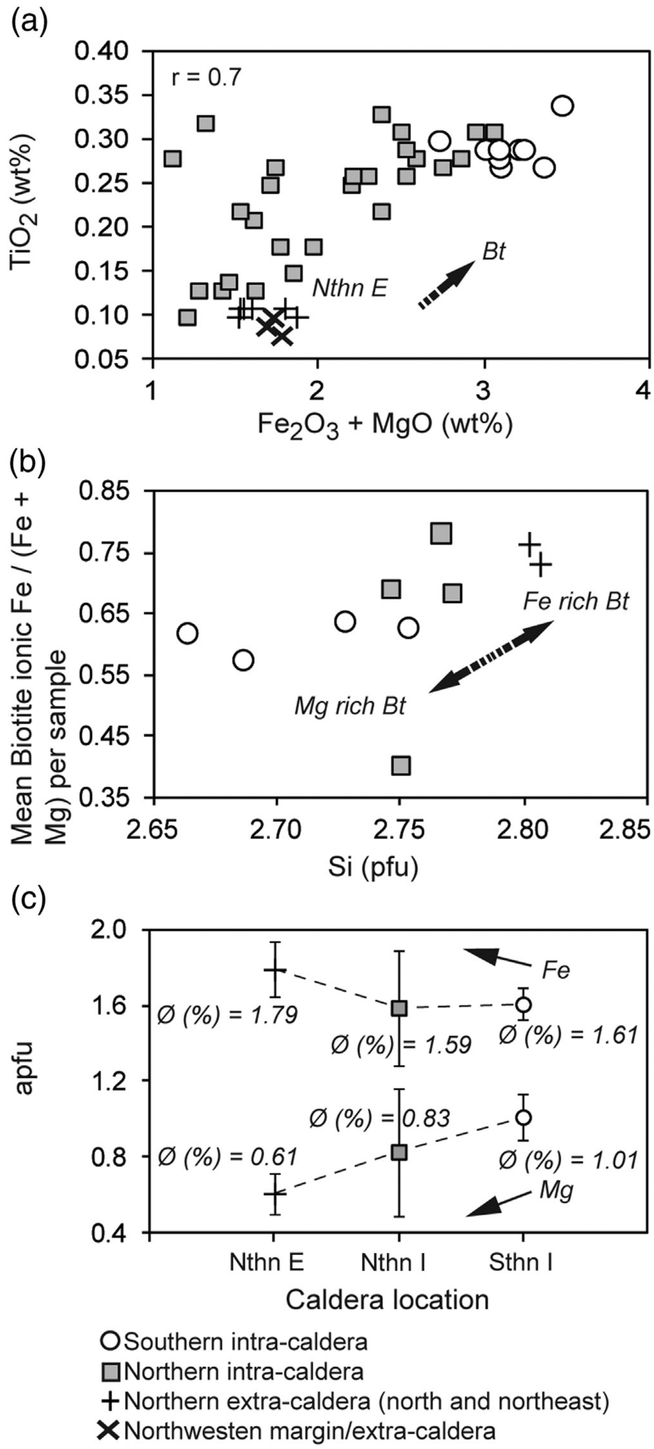

Fig. 15. Selected bulk-rock major element variation diagrams (normalised to 100% on an anhydrous basis), illustrating (a) crystal fractionation of biotite (Fe_2O_3 + MgO, and TiO_2). Note the positive correlation of the elements associated with biotite (Bt), highest in the Southern succession. (b) Biotite compositional change from Mg- to Fe-rich from the Southern to Northern succession, also shown in (c) depicting single crystal biotite compositional change (Mg and Fe/apfu) from the Southern to the Northern intra-caldera and northern extra-caldera successions. Error bars represent standard deviation as a %.

dividing the samples by caldera region. Interestingly, the north-western margin/extra-caldera fine-crystal-rich lapilli tuff lithofacies is shown to have a distinct pattern with lower values for the LRE and Eu elements and higher HREE than the other sample regions. Additionally, there is a rotation of the sample patterns with increased differentiation, common to other rhyolites, such as the Bishop Tuff (Hildreth, 1979; Barth et al., 1993).

4.5.2. Lateral and vertical variations

By dividing the bulk-rock data by region, subtle variation is revealed across the system. There is often a trend shown between the Southern samples and Northern samples, showing: (1) General northward system decline in Fe_2O_3, MgO, Na_2O, P_2O_5, Ce, Hf, Ba, V, Zr with TiO_2 and increase in SiO_2, K_2O, Rb, Y, and Nb with TiO_2 (Figs. 11, 12 and 14; Tables 3–5). Significantly, the HFS elements show similar separation of the samples by caldera region as the other elements (Fig. 12; Table 4). This is important due to their value in defining trends in altered rocks (Pearce and Norry, 1979), and therefore, offer evidence that the trends are primary. (2) A distinction of the Southern samples, with higher MgO, Na_2O, Nb, Ta and Y and lower K_2O, La, Ce, Ba, Hf, Th and Zr, at the same TiO_2 abundance to the Northern succession (Figs. 11 and 12). There is also a reduced compositional variation in the Southern samples, reflected by the lower standard deviations, particularly for the immobile HFS of Zr, Y, and Nb (Table 3). (3) The spread of the data is also shown to vary by caldera region. The Southern intra-caldera and northern extra-caldera samples generally form clusters. In contrast, the Northern intra-caldera samples display a greater spread, implying that the Northern succession may have been sourced from more evolved magma than the Southern succession (Fig. 11; Table 3). (4) Significantly, the Southern, Northern and northern extra-caldera samples (north and northeast, northwest) do not always show collinear trends, expressed particularly in the HFS elements in Fig. 12.

Fig. 14 shows representative major and trace element chemical data, together with biotite crystal fragments and total crystal fragment abundance data, plotted against stratigraphy. The dataset shows no systematic vertical chemical zonation between the stratigraphic sections. Furthermore, stratigraphic sections individually demonstrate varying levels of heterogeneity and local zonation, particularly in Sections 2, 3 and 4 in the Northern intra-caldera and intra-caldera ridge (Fig. 14b–c).

In summary, there is clear lateral compositional variation across the Southern, Northern and northern extra-caldera deposits. These results support the componentry and mineral point count data, discussed in Sections 4.1 and 4.3–4.4. The observed vertical variations illustrate compositional heterogeneity and local zonation, which broadly align with local temporal changes in lithofacies through some sections.

4.5.3. Biotite fractionation

The ignimbrite succession has been shown to have subtle variations in mineralogy and chemical composition, as outlined above. To isolate if this reflects primary magma compositional variation or an artefact of alteration or winnowing, major and trace elements were plotted to investigate the magmatic trends (Fig. 15).

A strong correlation is found on the diagram of TiO_2 with Fe_2O_3 + MgO ($r = 0.7$), with the Southern intra-caldera samples showing larger values of both, reflecting the high biotite abundance in this deposit (Fig. 15a; Table 2). Mean crystal fragment biotite Fe/(Fe + Mg) versus Si, varies by caldera region (Fig. 15b; bulk sample). The Southern intra-caldera biotite display lower Fe/(Fe + Mg), than the Northern intra-caldera and northern extra-caldera samples, changing from 0.57–0.78. This is consistent with the slightly more silica-rich, evolved bulk composition of the Northern deposits (Fig. 11g). Importantly, these data support the modal point count and bulk-rock chemical data. An outlier from the upper stratigraphy within the Northern intra-caldera succession is likely the result of increased alteration of its three biotite crystals analysed. Distinction between the Southern intra-caldera and Northern intra- and extra-caldera deposits is further shown by plotting the mean ionic Fe and Mg of analysed biotite crystal fragments (Fig. 15c). Fig. 15c illustrates that the Southern intra-caldera biotite population is more magnesium-rich (average 1.01) and generally less variable (lower standard deviation, dashed line error bars; Fig. 15c).

In summary, we conclude that the ignimbrite succession is rhyolitic and has a largely similar bulk composition. The mineralogical data shows subtle variations both vertically and across the deposits of the Northern and Southern caldera successions. This is particularly evident in the evolution trend across the system, reduced abundance of phenocryst and matrix crystal fragment biotite in the northern samples and sympathetic northwards bulk decreases of Na_2O + CaO and Fe_2O_3 + MgO, and increasing Fe-rich biotite. In conclusion, this data supports field observations and petrographic data, all of which indicate a less differentiated Southern ignimbrite succession and most evolved northern extra-caldera succession.

5. Discussion

Variations in componentry, mineralogical and chemical data, within this dominantly intra-caldera ignimbrite succession, can provide general insights into the subsurface magma source and withdrawal processes, and help decipher the eruption process. We will then discuss how the characteristics of the Ora caldera compare to other large caldera systems.

5.1. The Ora magma source

The Ora ignimbrite is homogenous over hundreds of metres of thickness. Detailed field description and laboratory analysis, nevertheless, revealed subtle horizontal and vertical heterogeneity in relation to componentry, mineralogy, bulk-rock and single mineral compositions (Figs. 9–13; Tables 2–5). These are summarized by the following:

(a) The Southern intra-caldera samples are less evolved (73–74.9% SiO_2 and higher Fe_2O_3, MgO, and TiO_2 values), richer in total crystal fragments (62%) and biotite abundance (12%). The samples are also compositionally distinct showing higher MgO, Na_2O, Nb, Ta and Y and lower K_2O, La, Ce, Ba, Hf, Th and Zr, at the same TiO_2 abundance to the Northern succession (Figs. 11 and 12).

(b) The Northern intra-caldera samples are slightly more evolved (72.5–76.9% SiO_2), with less total crystal fragments (55%) and biotite abundance (7%), and more compositionally variable.

(c) The northern extra-caldera samples (combined north, east, west) are shown to be the most evolved (76–77.7% SiO_2), with the lowest total crystal fragments (50%) and biotite abundances (2%; Fig. 11; Tables 2–4).

(ci.) The northwestern margin/extra-caldera fine-crystal-rich lapilli tuff deposit is shown to be subtly distinct from the other regions and ignimbrite lithofacies, displaying: a dominance of small-sized, fine juvenile clasts (Fig. 3f), increased abundance of sub-rounded phenocryst and crystal fragment morphologies (Fig. 4a and b (v)), a distinct crystal size distribution (Fig. 6); lower mean total matrix crystallinity (average 34%); displaying highly evolved quartz titanium values (Fig. 8b); and subtle chemical distinction shown by the major and trace elements, such as lower LREE and Eu and higher HREE values than the other samples (Figs. 11–14).

(d) The absence of uniform collinear trends between the Southern and Northern deposits.

(e) The non-systematic vertical mineralogical and element variation within depo-centres and across the system (Figs. 9, 12 and 14), indicating a lack of preserved single chamber zonation.

These features define subtle compositional differences between the Southern and Northern intra-caldera successions and also likely for the fine-crystal-rich lapilli-tuff lithofacies deposit, providing evidence that while very similar, they are likely not co-magmatic.

5.1.1. Origin of compositional heterogeneity

Compositional heterogeneity within large-volume, crystal-rich ignimbrite deposits has previously been related to eruption of a homogeneous magma, modified syn- and post-eruptively through physical processes, such as winnowing — e.g. the Fish Canyon Tuff (Whitney and Stormer, 1985). Alternatively, via eruption from a single heterogeneous magma source, e.g. the Toba Tuff (Chesner, 1998), or multiple related magma batches, e.g. Mangakino Volcanic Complex, TVZ, New Zealand (Briggs et al., 1993).

Accurate assessment of crystal enrichment in the Ora ignimbrite matrix crystal population by winnowing is difficult, due to the large variation in abundance of phenocrysts (0–60%) in juvenile clasts and crystal fragments (20–60%) in the matrix. Application of a model such as the enrichment factor (EF; Walker, 1972) could not be confidently undertaken due to the impossibility to physically separate out juvenile clasts. That said, point count comparison of the phenocryst and matrix crystal populations does show that crystal enrichment occurred (Table 6). For example, in the Northern coarse-crystal-rich lapilli-tuff lithofacies there is a mean of 28% phenocrysts to 58% crystal fragments, showing enrichment by a factor of 2 or more (Table 6). Although there was crystal enrichment in the deposit, we suggest that the winnowing process was not the main cause generating the observed deposit heterogeneity, based on the following lines of evidence:

(a) The moderate fine ash matrix content across the ignimbrite succession (average 35%).

(b) The systematic northwards decreases in modal phenocrystic biotite, reflecting similar trends in the matrix biotite crystal fragment population (Fig. 10). This is significant as phenocryst variations within juvenile clasts are not influenced by winnowing;

(c) The northwards change in composition of biotite crystal fragments, a feature also independent of winnowing (Fig. 15b and c);

(d) The absence of a Plinian fallout deposit;

(e) Complete deposit welding. However, the age of the deposit needs to be considered as it could mean any potential non-welded material may have been lost over time.

Table 6
Regional comparison of the phenocrysts in juvenile clasts and matrix crystal fragment abundances within the different Ora Formation ignimbrite lithofacies.

Region	Lithofacies	Mean	Median	St. dev.	Min.	Max.	*n*
Phenocrysts in juvenile clasts (n = 100)							
South	CCLT	26.7	27.8	10.7	10.0	49.0	16
South	CCLT: Bm	25.9	25.5	11.8	9.0	41.0	6
North	CCLT	27.8	27.0	10.8	12.0	57.7	31
North	CCLT: Bm	30.5	26.3	13.8	14.0	55.0	18
North	LRLT	17.7	15.5	6.1	13.0	24.7	3
North	FCLT	NA	NA	NA	NA	NA	NA
Nth Extra	CCLT	26.5	27.4	13.4	3.0	49.5	10
Nth Extra	FCLT	20.4	20.0	8.1	11.0	34.0	13
Crystal fragments within the matrix (n = 128)							
South	CCLT	62.2	62.4	4.0	49.0	69.0	25
South	CCLT: Bm	56.3	57.6	4.1	51.6	61.5	5
North	CCLT	58.4	58.6	6.0	47.9	70.5	39
North	CCLT: Bm	49.9	49.9	6.0	38.5	59.1	19
North	VLT	56.1	56.1	2.0	54.6	57.5	2
North	LRLT	56.1	56.6	7.1	48.6	66.8	5
North	FCLT	46.8	47.3	5.6	39.9	52.8	4
Nth Extra	CCLT	49.6	47.0	4.1	43.5	54.1	9
Nth Extra	VLT	52.3	52.7	2.1	49.7	54.2	4
Nth Extra	FCLT	47.1	45.8	4.8	40.6	53.4	9

* CCLT = coarse-crystal-rich lithofacies (Bm = bimodal crystal sub-facies), FCLT = fine-crystal-rich lithofacies, LRLT = lithic-rich lithofacies, VLT = vitrophyre lithofacies.
* Data represents normalised data (area % of crystal fragment to matrix, or phenocryst to groundmass only).

Combined, these factors indicate that winnowing processes were restricted both during eruption and from the tops of pyroclastic flow pulses. We therefore propose that winnowing was not the only factor contributing to the heterogeneity observed within the ignimbrite succession.

While there is a broad normal evolutionary trend shown across the deposit from south to north, the variations are not simple or easily explained by a single, simply zoned chamber. Therefore, we consider the more likely options for the deposit heterogeneity to be either eruption of genetically related subtly different magma batches within a reservoir network or eruption of discrete melt pockets within a single heterogeneous chamber. The magma heterogeneity was most likely produced via fractional crystallisation and assimilation processes at depth during magma ascent and residence in the upper crustal magma chamber network. Beyond the large-scale northwards decline in $MgO + Fe_2O_3$, and modal proportions and chemistry of biotite (Figs. 10–12), this is indicated by the general enrichment of La, Ce, Th and depletion of Nb, Zr and Y (Figs. 11 and 12), Eu anomaly, and scatter on the variation diagrams (Barth et al., 1993; Timmerman, 2004). The lack of evidence for a strong compositional zonation preserved within the deposit, together with the large magma volume and high crystallinity, suggests that sidewall crystallisation and fractionation processes were not dominant within the system (Christiansen, 2005). Alternatively, that evidence of such processes were lost during eruption and ignimbrite emplacement (Cashman and Giordano, 2014).

5.1.2. Magma withdrawal

In Sections 5.1–5.1.1 we summarized the main difference in samples taken across the caldera deposit, concluding that the deposit heterogeneity was chiefly produced by involvement of subtly different magma batches (Figs. 9–15; Tables 2–4). A number of models could account for the deposit architecture:

(1) simultaneous tapping of a complex of magma reservoirs, with mutual or separate conduits, or eruption from a late-stage amalgamated chamber (Cashman and Giordano, 2014), e.g. the Snake River Plain rhyolite (Ellis et al., 2010);
(2) co-eruption of different regions or levels within a single zoned magma chamber, e.g. the Bishop tuff and Whakamaru group ignimbrites (Fridrich and Mahood, 1987; Brown et al., 1998; Hildreth and Wilson, 2007);
(3) eruption of different magmas from a single magma chamber, due to injection of hot magma(s) with differing crystallinity and composition into the lower temperature partially crystallised magma, e.g., the Cerro Galan ignimbrite, Huaynaputina Volcano, and Fish Canyon Tuff (Bachmann et al., 2005; de Silva et al., 2008; Wright et al., 2011)

The juvenile clast, mineralogical, and chemical variations, together with the stratigraphic-compositional architecture of the ignimbrite suggest a pene-contemporaneous tapping of a complex magma reservoir. All three models allow explanation of the preserved features of the Ora ignimbrite, however, we believe that the most likely option is model 1. This involves eruption from a genetically related, interconnected magma reservoir, where melt was stored prior to eruption across a number of chambers, subsequently tapped during eruption, producing the observed deposit variations. While further data is needed to constrain this model, this builds on the work of Barth et al. (1992, 1993) who propose as MASH type (Hildreth and Moorbath, 1988) model for the larger Athesian Volcanic Group, with multiple magma chambers between the lower and upper crust. Moreover, such a pre-eruptive magma chamber network is consistent with recent models such as that of Cashman and Giordano (2014). A single zoned chamber, perhaps either with a crystal-rich 'mush-like' dense base/outer zone and more evolved crystal-poor middle/upper zone (e.g. Barth et al., 1993), or discrete melt pockets due to successive melt injections, would require a reverse tapping of the magma chamber, to produce the less evolved, crystal-rich Southern succession first, progressing to eruption of the more evolved, less crystal-rich Northern succession (discussed in Section 5.2). A reverse withdrawal model is common for ignimbrite eruptions (e.g. Grizzly Peak eruption, USA; Fridrich and Mahood, 1987) and shown in recent theoretical modelling (Gudmundsson, 2012a,b), however, we believe in this instance, that it is the less likely option for this eruption.

5.2. Caldera eruption processes

5.2.1. Caldera collapse and eruption evolution

A single large caldera collapse event does not adequately explain our findings with regards to the lateral and vertical compositional variations of the Ora system, together with the known stratigraphic architecture (Willcock et al., 2013). Instead, we infer a two-stage history.

In stage 1, caldera collapse and eruption was initiated in the south of the system forming the Southern intra-caldera and extra-caldera deposits. This is possibly the combined result of the extensional environment during the Permian and utilisation of pre-existing crustal weaknesses, as has also been suggested for previous Athesian Volcanic Group caldera-forming events (Marocchi et al., 2008; Morelli et al., 2010).

In stage 2, a second major caldera collapse and eruption event occurred, forming the Northern intra-caldera and extra-caldera deposits. This second caldera-forming stage with associated source vent(s) migration, was likely a result of the loss of magma volume during the Southern caldera eruption, causing instability and foundering of the chamber roof in the northern part of the system (Willcock et al., 2013, 2014). This collapse process produced two nested, pene-contemporaneous caldera depressions (Fig. 1c).

The combined mineralogical, geochemical and lithofacies variations can importantly be used to define the eruption chronology. This is complex however, due to the absence of samples from the northern region of the Southern caldera, lack of clear correlation in lithofacies between the nested depressions, and absence of preserved overlap in relation to lithofacies or bulk chemistry of either intra-caldera succession on the other. A south to north eruption evolution is based on the mineralogical and chemical compositional differences across the succession (Figs. 9–15), and the following specific observations: (1) the interleaving of lithofacies up the northern margin of the Northern caldera and textural correlation and progression over the margin. Together with interleaving of lithofacies up the intra-caldera ridge, and southern margin of the Southern caldera (Willcock et al., 2013). These relationships suggest late-stage filling and over-spilling of deposits into the extra-caldera setting. (2) the most evolved deposits residing outside the Northern caldera. If this represented the initial products of the eruption, there would have needed to have been an initial low volume eruption without collapse, followed by major collapse and infilling of the subsided depression. The Northern deposit has three main features which suggest this did not occur. Firstly, the absence of evidence for a Plinian precursor deposit within the Northern extra-caldera. Secondly, the lack of lithofacies correlation between the base of the Northern intra-caldera fill lithofacies and northern extra-caldera lithofacies. This is shown at the basal exposure in the Northern intra-caldera, with the occurrence of the lag breccia and the lithic-rich lapilli-tuff lithofacies (Willcock et al., 2013). Thirdly, the limited (preserved) volume of extra-caldera material.

5.2.2. Eruption intensity and vent migration

Textural comparison of the size and shape of phenocrysts (whole and fractured) and matrix crystal fragment populations can provide insight into the relative explosive intensity and mechanisms of volcanic eruption (e.g. Best and Christiansen, 1997; Allen and McPhie, 2003).

In the Ora succession, whole phenocrysts are more commonly euhedral to subhedral, with the occurrence of some internally ruptured phenoclast-like phenocrysts (Figs. 4a and 5a–b; Best and Christiansen, 1997). In contrast, crystal fragments are typically subhedral to anhedral (Fig. 4b). This data is suggestive of explosive fragmentation during the eruptive phase and little subsequent abrasion of crystals during transport. While these variations are to be expected, the shape comparison of the two populations is useful when compared with the crystal size distribution information. Figs. 4 and 6 highlight that the sub-grains of the phenocrysts are comparable in size (common 0.5 to 4 mm crystals) and shape to the variably fragmented crystal fragments. This implies that the difference between the two is unrelated to the degree of fracturing, but rather reflects wider disintegration of fractured grains in the matrix. Importantly, this supports the hypothesis of a relatively low energy, low eruption column collapse model for this caldera system (Willcock et al., 2013), causing minimal further fragmentation of phenocrysts during eruption, pyroclastic flow transport and deposition.

In some stratigraphic sections, base-to-top compositional variation shows local correlation with lithofacies changes (Figs. 9 and 14). These data, combined with image analysis of crystal size variations in the different ignimbrite lithofacies (e.g. Figs. 4b and 6), support key hypotheses. Firstly, that multiple flow pulses aggraded during eruption, recording variations in available source material, both in chemical composition and componentry, and secondly, that caldera eruption occurred as a result of eruption from multiple source locations (Figs. 9 and 14; Willcock et al., 2013, 2014). If this succession had been erupted from a single source location, we would expect greater correlation between lithofacies and a 'layer cake' structure throughout the intra-caldera fill, which is not the case (Willcock et al., 2013).

5.3. Caldera comparison

The Ora caldera system does not neatly conform to either a typical zoned rhyolitic system, or a monotonous dacitic system (Table 7). Instead it has features intermediate between these two end-members. It displays a number of features characteristic of dacitic systems, such as a restricted composition, a high crystallinity, and an absence of a Plinian precursor phase. While also having a rhyolitic composition and displaying internal lateral variation. This mix of features is not unique to the Ora caldera, also shown for example in the Yellowstone caldera system (Christiansen, 2001) and Toba caldera (Chesner, 1998). This highlights the variation in natural caldera systems and difficulty in caldera classification (Marti et al., 2008), and understanding of eruption processes and significantly, hazard management.

Importantly, this large, crystal-rich caldera system does not conform to the typical two-stage caldera eruption process (Druitt and Sparks, 1984), as it lacks the Plinian fallout phase. Such caldera systems are less commonly reported in the literature, however, with the addition of the Ora caldera, appear to be more common than previously thought. These systems have a distribution across many continents, including Europe, South America, North America, and Australia. They form under a number of (predominantly extensional) tectonic conditions and are also found to occur during different periods of Earth's history from the Ordovician to late Devonian (Clemens and Wall, 1984; McLaughlin, 1988; Gaul, 1995; Beddoe-Stephens and Millward, 2000; Wang et al., 2001; Birch, 2003; Cas et al., 2003), Permian (current study; Marti, 1991, 1996; Quick et al., 2009), in a number of Tertiary systems clustered in the USA and Mexico (Lipman, 1976, 1984; Bachmann et al., 2000, 2002; Aguirre-Díaz and Labarthe-Hernañdez, 2003; Best et al., 2013), and some Tertiary to Quaternary systems in the Andes

Table 7
Comparison of the Ora caldera system with a selection of other large caldera systems globally.

Ignimbrite	Caldera	Period	Composition	Volume (km^3)	Zonation	Crystallinity	Plinian precursor	Example workers
Ora ignimbrite, Italy	Ora	Permian	Rhyolitic	>1290	No Some Heterogeneity Reason: different magma packages	~20–57%	No	Current study
Caetano Tuff, USA	Caetano	Eocene (Tertiary)	Rhyolitic	>1100	Yes—Weak normal	35–50%	No	John et al. (2008), MacDonald et al. (2012)
Cottonwood Wash Tuff, USA	Caldera unknown, Indian Peak Complex	Oligocene (Tertiary)	Dacitic	2000	No	>20%	No	Best and Christiansen (1997), Best et al. (2013)
Wah Wah Springs Tuff, USA	Indian Peak Complex	Oligocene (Tertiary)	Dacitic	5900	No	>20%	No	Best et al. (2013)
Lund Tuff, USA	White rock, Indian Peak Complex	Oligocene (Tertiary)	Dacitic	4400	No Some heterogeneity Reason: different magma packages	>20%	No	Best et al. (1989), Maughan et al. (2002), Christiansen (2005), Best et al. (2013)
Fish Canyon Tuff, USA	La Garita,	Oligocene (Tertiary)	Dacitic	5000	No Some heterogeneity Reason: winnowing	40–54%	Debated	Whitney & Stormer (1985), Bachmann and Bergantz (2003), Lipman (2007)
Cerro Galan ignimbrite, Argentina	Cerro Galan	Quaternary	Dacitic	630	No	55%	No	Francis et al. (1983, 1989), Sparks et al. (1985), Folkes et al. (2011a,b)
Huckleberry ridge Tuff, USA	Yellowstone Complex	Quaternary	Rhyolitic	2450	Yes—Normal	0–20%	Yes	Christiansen (2001), Girard and Stix (2012)
Bandelier Tuff, USA	Toledo/Valles	Quaternary	Rhyolitic	300	Yes—Reverse	<40%	Yes	Smith and Bailey (1966), Wolff et al. (2011)
Bishop Tuff, USA	Long Valley	Quaternary	Rhyolitic	600	Yes—Normal	1–24%?	Yes	Hildreth (1979), Palmer et al. (1996), Hildreth and Wilson (2007)
Lava Creek Tuff, USA	Yellowstone Complex	Quaternary	Rhyolitic	1000	Yes—Normal	15–35%	Debated	Christiansen (2001), Girard and Stix (2012)
Whakamaru Group ignimbrites, New Zealand	Taupo Volcanic Zone	Quaternary	Rhyolitic	~2500	Yes—Reverse	~10–35%	Debated	Houghton et al. (1995), Brown et al. (1998)
Toba Tuff (YTT), Indonesia	Toba	Quaternary	Rhyolitic	2000	Yes—Weak normal	35–50%	Yes	Knight et al. (1986), Chesner (1998, 2012), Gardner et al. (2002)

(Francis et al., 1983; Sparks et al., 1985; Lindsay et al., 2001; de Silva et al., 2006; Folkes et al., 2011b).

6. Conclusions

The preservation of the largely intra-caldera Ora ignimbrite succession provides a unique opportunity to study its chemical architecture, gain insight into the pre-eruptive magma system and propose a model for the caldera eruption evolution. The ignimbrite deposit has a rhyolitic composition, a compositional range between 72.5–77.7% SiO_2, is generally crystal-rich, and has variable phenocryst contents in juvenile clasts. The succession has measureable horizontal and vertical variations in modal mineral and chemical composition.

We conclude;

1. The Ora Formation ignimbrite succession displays subtle but detectable major and trace element ranges, consistent with an eruption from a heterogeneous magma system.
2. The chemical and mineralogical data reveal important compositional differences between the Southern and Northern deposits and northwestern extra-caldera deposit, suggesting magma differentiation across the caldera system. The upper crustal Ora magma system is proposed as being comprised of a genetically related, multi-chambered magma reservoir network, where multiple chambers were tapped during eruption to produce the deposit variation.
3. The chemistry and mineralogy trends, together with the stratigraphic architecture (Willcock et al., 2013), suggest that caldera collapse and eruption progressed from south to north. Bulk-rock geochemistry data suggest the Southern succession was sourced from a less fractionated, crystal-rich source, while the Northern succession was from a more evolved source region. The latter stages of the eruption are preserved by the outpouring of material in the northern extra-caldera setting, which has the most evolved chemical signature and subtly distinct fine-crystal-rich lapilli-tuff lithofacies deposit.
4. Mineralogical and compositional data illustrates heterogeneity and local zonation from base-to-top of the main intra-caldera and extra-caldera successions. These variations, together with matrix crystal fragment size variations between ignimbrite lithofacies, support the hypothesis of a multi-vent eruption process, incremental caldera in-filling by subtly compositionally different pyroclastic flow pulses, and a lower intensity eruption style (Willcock et al., 2013, 2014).

Acknowledgements

We would like to thank the Department of Biological, Geological and Environmental Sciences (BiGeA), University of Bologna, for their research collaboration and analysis work and the efforts of Dr. Corrado Morelli and the Ufficio Geologia e Prove materiali of the Provincia Autonoma di Bolzano Südtirol for logistical support. We would also like to thank A/Prof. Malcolm Wallace and Dr Massimo Raveggi for their analytical support. Furthermore, we thank Prof. Peter Lipman, Prof. Jocelyn McPhie, Prof. Eric Christiansen, Dr Joan Andújar, Marion Anderson and Julie Boyce for their useful comments on the manuscript. This work has been partially funded by an Australian Postgraduate Award and by discretionary research grants of Ray Cas.

References

Acocella, V., 2008. Structural Development of Calderas: A Synthesis from Analogue Experiments. Elsevier.
Aguirre-Díaz, G., Labarthe-Hernañdez, G., 2003. Fissure ignimbrites: fissure-source origin for voluminous ignimbrites of the Sierra Madre Occidental and its relationship with basin and range faulting. Geology 31, 773–776.
Allen, S.R., Mcphie, J., 2003. Phenocryst fragments in rhyolitic lavas and lava domes. J. Volcanol. Geotherm. Res. 126, 263–283.
Bachmann, O., Bergantz, G.W., 2003. Rejuvenation of the Fish Canyon magma body: a window into the evolution of large-volume silicic magma systems. Geology 31, 789–792.
Bachmann, O., Bergantz, G.W., 2006. Gas percolation in upper-crustal magma bodies as a mechanism for upward heat advection and rejuvenation of silicic crystal mushes. J. Volcanol. Geotherm. Res. 149, 85–102.
Bachmann, O., Bergantz, G.W., 2008. Rhyolites and their source mushes across tectonic settings. J. Petrol. 49, 2277–2285.
Bachmann, O., Dungan, M.A., Lipman, P.W., 2000. Voluminous lava-like precursor to a major ash-flow tuff: low-column pyroclastic eruption of the Pagosa Peak Dacite, San Juan Volcanic Field Colorado. J. Volcanol. Geotherm. Res. 98, 153–171.
Bachmann, O., Dungan, M.A., Lipman, P.W., 2002. The Fish Canyon magma body, San Juan Volcanic Field, Colorado: rejuvenation and eruption of an upper-crustal batholith. J. Petrol. 43, 1469–1503.
Bachmann, O., Dungan, M.A., Bussy, F., 2005. Insights into shallow magmatic processes in large silicic magma bodies: the trace element record in the Fish Canyon magma body, Colorado. Contrib. Mineral. Petrol. 149, 338–349.
Bargossi, G.M., D'Amico, C., Segatta, G., 1983. Vulcaniti Atesine in serie ridotta ad est di Trento. Mineral. Petrogr. Acta 27, 207–219.
Bargossi, G.M., Mair, V., Morelli, C., Sapelza, A., 1999. The Athesian Volcanic District (Bolzano-Trento area): a general outline. Field Trip Book, International Field Conference on 'The Continental Permian of the Southern Alps and Sardinia (Italy), Brescia'.
Bargossi, G.M., Klötzli, U., Mair, V., Marocchi, M., Morelli, C., 2004. The Lower Permian Athesian Volcanic Group (AVG) in the Adige valley between Merano and Bolzano: a stratigraphic, petrographic and geochronological outline. 32 IGC Abstractp. 187 (1 part 1).
Bargossi, G.M., Mair, V., Marocchi, M., Morelli, C., Moretti, A., Piccin, G., 2007. A mega volcano-tectonic collapse between Bolzano and Trento during the Lower Permian. Mitt. Österr. Mineral. Ges. 153, 34.
Barth, S., 1994. Calc-alkaline basic to silicic rock suites from the Late Hercynian Atesina–Cima d'Asta volcano–plutonic complex (Southern Alps, N Italy): evidence for the primary magmatic and hydrothermal alteration processes. N. Jb. Mineral. (Abh.) 168, 15–46.
Barth, S., Oberli, F., Meier, M., Blattner, P., Bargossi, G.M., Di Battistini, G., 1992. Nd-Sr isotope evidence for mantle-crust interaction: a study of the Late Hercynian calc-alkaline Atesina-Cima d'Asta volcano-plutonic complex. N Italy. 29th Int. Geol. Congr IGC, 2.
Barth, S., Oberli, F., Meier, M., Blattner, P., Bargossi, G.M., Di Battistini, G., 1993. The evolution of a calc-alkaline basic to silicic magma system: geochemical and Rb–Sr, Sm–Nd and $^{18}O/^{16}O$ isotopic evidence from the Late Hercynian Atesina–Cima d-Asta volcano–plutonic complex, northern Italy. Geochim. Cosmochim. Acta 57, 4285–4300.
Beddoe-Stephens, B., Millward, D., 2000. Very densely welded, rheomorphic ignimbrites of homogeneous intermediate calc-alkaline composition from the English Lake District. Geol. Mag. 137, 155–171.
Berger, C., Satir, M., 1991. New geochemical data for the Permian–Carboniferous Bolzano volcanics (Val Gardena, N-Italy). Eur. J. Mineral. 3, 29 (abstr.).
Best, M.G., Christiansen, E.H., 1997. Origin of broken phenocrysts in ash-flow tuffs. Geol. Soc. Am. Bull. 109, 63–73.
Best, M.G., Christiansen, E.H., Blank, R.H., 1989. Oligocene caldera complex and calc-alkaline tuffs and lavas from the Indian Peak volcanic field, Nevada and Utah. Geol. Soc. Am. Bull. 101, 1076–1090.
Best, M.G., Christiansen, E.H., Deino, A.L., Gromme, S., Hart, G.L., Tingey, D.G., 2013. The 36–18 Ma Indian Peak — Caliente ignimbrite field and calderas, southeastern Great Basin, USA: multicyclic super-eruptions. Geosphere 9, 864–950.
Bindeman, I.N., 2006. The secrets of supervolcanoes: microscopic crystals of volcanic ash are revealing surprising clues about the world's most devastating eruptions. Sci. Am. 38–43.
Birch, W.D., 2003. The geology of Victoria. Geol. Soc. Aust. Spec. Publ. 23.
Bonin, B., Brandlein, P., Bussy, F., Desmons, J., Eggenberger, U., Finger, F., Graf, K., Marro, C., Mercolli, I., Oberhansli, R., Ploquin, A., Von Quadt, A., Von Raumer, J.F., Schaltegger, U., Steyrer, H.P., Visona, D., Vivier, G., 1993. Late Variscan Magmatic Evolution of the Alpine Basement. Springer-Verlag, Berlin New York.
Boynton, W.V., 1985. Chapter 3: cosmochemistry of the rare earth elements: meteorite studies. In: Henderson, P. (Ed.), Rare Earth Element Geochemistry. Elsevier, Amsterdam.
Branney, M.J., Kokelaar, P., 2002. Pyroclastic density currents and the sedimentation of ignimbrites. Geol. Soc. Lond. Mem. 27, 143.
Briggs, R.M., Gifford, M.G., Moyle, A.R., Taylor, S.R., Norman, M.D., Houghton, B.F., Wilson, C.J.N., 1993. Geochemical zonation and eruptive mixing in ignimbrites from the Mangakino volcano, Taupo Volcanic Zone, New Zealand. J. Volcanol. Geotherm. Res. 56, 175–203.
Brown, S.J.A., Wilson, C.J.N., Cole, J.W., Wooden, J., 1998. The Whakamaru group ignimbrites, Taupo Volcanic Zone, New Zealand: evidence for reverse tapping of a zoned silicic magmatic system. J. Volcanol. Geotherm. Res. 84, 1–37.
Cas, R.A.F., O'Halloran, G.J., Long, J.A., Vandenberg, A.H.M., 2003. Middle Devonian to Carboniferous, Melbourne. Geol. Soc. Aust. Spec. Publ. 23.
Cas, R.A.F., Giordano, G., Marti, J., 2012. Using the stratigraphic record to understand the nature of caldera collapse (incremental vs catastrophic), the way calderas are constructed, and the contrasting spatial and temporal scales for big and small calderas. IAVCEI Caldera Collapse Workshop 2012. Bolsena, Italy.
Cashman, K.V., Giordano, G., 2014. Calderas and magma reservoirs. J. Volcanol. Geotherm. Res. 288, 28–45.
Cassinis, G., Perotti, C.R., 2007. A stratigraphic and tectonic review of the Italian Southern Alpine Permian. Palaeoworld 16, 140–172.
Cassinis, G., Perotti, C.R., Ronchi, A., 2012. Permian continental basins in the Southern Alps (Italy) and peri-Mediterranean correlations. Int. J. Earth Sci. (Geol. Rundsch.) 101, 129–157.

Castellarin, A., Cantelli, L., 2000. Neo-Alpine evolution of the Southern Eastern Alps. J. Geodyn. 30, 251–274.
Charlier, B.L.A., Bachmann, O., Davidson, J.P., Dungan, M.A., Morgan, D.J., 2007. The upper crustal evolution of a large silicic magma body: evidence from crystal-scale Rb–Sr isotopic heterogeneities in the Fish Canyon magmatic system, Colorado. J. Petrol. 48, 1875–1894.
Chesner, C.A., 1998. Petrogenesis of the Toba Tuffs, Sumatra. J. Petrol. 39, 397–438.
Chesner, C.A., 2012. The Toba Caldera Complex. Quat. Int. 258, 5–18.
Christiansen, R.L., 2001. The Quaternary and Pliocene Yellowstone Plateau Volcanic Field of Wyoming, Idaho, and Montana. U. S. Geol. Surv. Prof. Pap. 729-G, 145.
Christiansen, E.H., 2005. Contrasting processes in silicic magma chambers: evidence from very large volume ignimbrites. Geol. Mag. 142, 669–681.
Christiansen, R.L., Lipman, P.W., Carr, W.J., Byers Jr., F. M., Orkild, P. P. & Sargent, K. A., 1977. Timber Mountain–Oasis Valley caldera complex of southern Nevada. Geol. Soc. Am. Bull. 88, 943–959.
Clemens, J.D., Wall, V.J., 1984. Origin and evolution of a peraluminous silicic ignimbrite suite: the Violet Town Volcanics. Contrib. Mineral. Petrol. 88, 354–371.
Cole, J.W., Milner, D.M., Spinks, K.D., 2005. Calderas and caldera structures: a review. Earth Sci. Rev. 69, 1–26.
D'Amico, C., Del Moro, A., 1988. Permian and Triassic Rb–Sr dating in the Permian rhyodacitic ignimbrites of Trentino (Southern Alps). Rend. Soc. Ital. Mineral. Petrol. 43, 171–180.
D'Amico, C., Del Moro, A., Freddo, A., Pardini, G., 1980. Studio radiometrico delle ignimbriti riolitiche Atesine, Gruppo Superiore. Rend. Soc. Geol. Ital. 36, 703–716.
De Silva, S.L., Francis, P.W., 1989. Correlation of large ignimbrites — two case studies from the central Andes of northern Chile. J. Volcanol. Geotherm. Res. 37, 133–149.
De Silva, S.L., Gosnold, W.D., 2007. Episodic construction of batholiths: insights from the spatiotemporal development of an ignimbrite flare-up. J. Volcanol. Geotherm. Res. 167, 320–335.
De Silva, S.L., Zandt, G., Trumbell, R., Viramonte, J.G., Salas, G., Jimenez, N., 2006. Large ignimbrite eruptions and volcano-tectonic depressions in the Central Andes: a thermomechanical perspective. Mechanisms of Activity and Unrest at Large Calderas, 269, 47–63.
De Silva, S., Salas, G., Schubring, S., 2008. Triggering explosive eruptions — the case for silicic magma recharge at Huaynaputina, southern Peru. Geology 36, 387–390.
Druitt, T.H., Sparks, R.S.J., 1984. On the formation of calderas during ignimbrite eruptions. Nature 310, 679–681.
Ekren, E.B., Anderson, R.E., Rogers, C.L., Noble, D.C., 1971. Geology of the northern Nellis A.F.B. Bombing and Gunnery Range, Nye County, Nevada. U. S. Geol. Surv. Prof. Pap. 651, 91 pages.
Ellis, B.S., Wolff, J.A., 2012. Complex storage of rhyolite in the central Snake River Plain. J. Volcanol. Geotherm. Res. 211–212, 1–11.
Ellis, B.S., Barry, T., Branney, M.J., Wolff, J.A., Bindeman, I.N., Wilson, R., Bonnichsen, B., 2010. Petrologic constraints on the development of a large-volume, high temperature, silicic magma system: the Twin Falls eruptive centre, central Snake River Plain. Lithos 120, 475–489.
Folkes, C.B., De Silva, S.L., Wright, H.M., Cas, R.A.F., 2011a. Geochemical homogeneity of a long-lived, large silicic system; evidence from the Cerro Galán caldera, NW Argentina. Bull. Volcanol. 73, 1455–1486.
Folkes, C.B., Wright, H.M., Cas, R.A.F., De Silva, S., Lesti, C., Viramonte, J.G., 2011b. A reappraisal of the stratigraphy and volcanology of the Cerro Galán volcanic system, NW Argentina. Bull. Volcanol. 73, 1427–1454.
Francis, P.W., O'Callaghan, L., Kretschmar, G.A., Thorpe, R.S., Sparks, R.S.J., Page, R.N., De Barrio, R.E., Gillou, G., Gonzalez, O.E., 1983. The Cerro Galan ignimbrite. Nature 301.
Francis, P.W., Sparks, R.S.J., Hawkesworth, C.L., Thorpe, R.S., Pyle, D.M., Tail, S.R., Mantonvani, M.S., McDermott, F., 1989. Petrology and geochemistry of the Cerro Galan caldera, northwest Argentina. Geol. Mag. 126, 515–547.
Freundt, A., 1998. The formation of high-grade ignimbrites, part I: experiments on high- and low-concentration transport systems containing sticky particles. Bull. Volcanol. 59, 414–435.
Fridrich, C.J., Mahood, G.A., 1987. Compositional layering in the zoned magma chamber of the Grizzly Peak Tuff. Geology 15, 299–303.
Gardner, J.E., Layer, P.W., Rutherford, M.J., 2002. Phenocrysts versus xenocrysts in the Youngest Toba tuff: implications for the petrogenesis of 2800 km^3 of magma. Geology 30, 347–350.
Gaul, A. J. 1995. Geology of the Tolmie Highlands Igneous Complex. Melbourne: Unpublished PhD thesis, Monash University.
Gifkins, C., Herrmann, W., Large, R., 2005. Altered Volcanic Rocks: A Guide to Description and Interpretation. CODES, Hobart.
Girard, G., Stix, J., 2012. Future volcanism at Yellowstone caldera: insights from geochemistry of young volcanic units and monitoring of volcanic unrest. GSA Today Bull. 22, 4–10.
Gravley, D.M., Wilson, C.J.N., Leonard, G.S., Cole, J.W., 2007. Double trouble: paired ignimbrite eruptions and collateral subsidence in the Taupo Volcanic Zone, New Zealand. Geol. Soc. Am. Bull. 119, 18–30.
Gregg, P.M., De Silva, S.L., Grosfils, E.B., Parmigiani, J.P., 2012. Catastrophic caldera-forming eruptions: thermomechanics and implications for eruption triggering and maximum caldera dimensions on Earth. J. Volcanol. Geotherm. Res. 241–242, 1–12.
Gudmundsson, A., 2008. Magma-chamber Geometry, Fluid Transport, Local Stresses and Rock Behaviour during Caldera Collapse Formation. Elsevier.
Gudmundsson, A., 2012a. Magma chambers: formation, local stresses, excess pressures, and compartments. J. Volcanol. Geotherm. Res. 237–238, 19–41.
Gudmundsson, A., 2012b. Caldera collapses and magma-chamber compartments. IAVCEI Caldera Collapse Workshop, Bolsena, Italy.
Gudmundsson, M.T., Pedersen, R., Vogfjord, K., Thorbjarndottir, B., Jakobsdottir, S., Steinunn, R.M.J., 2010. Eruption of Eyjafjallajokull Volcano, Iceland. EOS Trans. Am. Geophys. Union 91, 190–191.
Hildreth, W., 1979. The Bishop Tuff: evidence for the origin of compositional zonation in silicic magma chambers. Colorado, Geological Society of America, Special Publication vol. 180.
Hildreth, W., 1981. Gradients in silicic magma chambers: implications for lithospheric magmatism. J. Geophys. Res. 86, 10153–10192.
Hildreth, W., 2004. Volcanological perspectives on Long Valley, Mammoth Mountain and Mono Craters: several contiguous but discrete systems. J. Volcanol. Geotherm. Res. 136, 169–198.
Hildreth, W., Moorbath, S., 1988. Crustal contributions to arc magmatism in the Andes of Central Chile. Contrib. Mineral. Petrol. 98, 455–489.
Hildreth, W., Wilson, C.J.N., 2007. Compositional zoning of the Bishop Tuff. J. Petrol. 48, 951–999.
Houghton, B.F., Wilson, C.J.N., Mcwilliams, M., Lanphere, M.A., Weaver, S.D., Briggs, R.M., Pringle, M.S., 1995. Chronology and dynamics of a large silicic magmatic system: Central Taupo Volcanic Zone, New Zealand. Geology 23, 13–16.
Huber, C., Bachmann, O., Dufek, J., 2012. Crystal-poor versus crystal-rich ignimbrites: a competition between stirring and reactivation. Geology 40, 115–118.
Janoušek, V., Farrow, C.M., Erban, V., 2006. Interpretation of whole-rock geochemical data in igneous geochemistry: introducing Geochemical Data Toolkit (GCDkit). J. Petrol. 47, 1255–1259.
Jellínek, A.M., Depaolo, D.J., 2003. A model for the origin of large silicic magma chambers: precursors of caldera-forming eruptions. Bull. Volcanol. 65, 363–381.
John, D.A., 1995. Tilted middle Tertiary ash-flow calderas and subjacent granitic plutons, southern Stillwater Range, Nevada: cross sections of an Oligocene igneous centre. Geol. Soc. Am. Bull. 107, 180–200.
John, D.H., Henry, C.D., Colgan, J.P., 2008. Magmatic and tectonic evolution of the Caetano caldera, north-central Nevada: a tilted, mid-Tertiary eruptive centre and source of the Caetano Tuff. Geosphere 4, 75–106.
Knight, M.D., Walker, G.P.L., Ellwood, B.B., Diehl, J.F., 1986. Stratigraphy, paleomagnetism, and magnetic fabric of the Toba Tuffs: constraints on the sources and eruptive styles. J. Geophys. Res. 91, 355–382.
Kretz, R., 1983. Symbols for rock-forming minerals. Am. Mineral. 68, 277–279.
Lamonica, C. R. 2012. Studio mineralogico, petrographico e geochimico delle facies ignimbritiche intra- ed extra-calderiche della Formazione di Ora del Gruppo Vulcanico Atesino (Permiano inferiore). Trentino-Alto Adige, Italia. Unpub. thesis, Alma Mater Studiorum University of Bologna, Italy.
Larsen, B.T., Olaussen, S., Sundvoll, B., Heeremans, M., 2008. The Permo-Carboniferous Oslo Rift through six stages and 65 million years. Episodes 31, 52–58.
Le Bas, M.J., Le Maitre, R.W., Streckeisen, A., Zanettin, B., 1986. Chemical classification of volcanic-rocks based on the total alkali silica diagram. J. Petrol. 27, 745–750.
Le Maitre, R.W., Bateman, P., Dudek, A., Keller, J., Lameyre Le Bas, M. J., Sabine, P. A., Schmid, R., Sorenson, H., Streckeisen, A., Woolley, A. R. & Zanettin, B., 1989. A Classification of Igneous Rocks and Glossary of Terms. Blackwell, Oxford.
Le Maitre, R.W., Streckeisen, A., Zanettin, B., Le Bas, M.J., Bonin, B., Bateman, G., Bellieni, G., Dudek, A., Efremova, S., Keller, J., Lameyre, J., Sabine, P.A., Schmid, R., Sorenson, H., Woolley, A.R., 2002. Igneous Rocks: A Classification and Glossary of Terms. Cambridge University Press.
Lesti, C., Porreca, M., Giordano, G., Mattei, M., Cas, R.A.F., Wright, H.M., Folkes, C.B., Viramonte, J.G., 2011. High-temperature emplacement of the Cerro Galán and Toconquis Group ignimbrites (Puna Plateau, NW Argentina) determined by TRM analyses. Bull. Volcanol. 73, 1535–1565.
Lindsay, J.M., Schmitt, A.K., Trumbull, R.B., De Silva, S.L., Siebel, W., Emmermann, R., 2001. Magmatic evolution of the La Pacana Caldera System, Central Andes, Chile: compositional variation of two cogenetic, large-volume felsic ignimbrites. J. Petrol. 42, 459–486.
Lipman, P.W., 1976. Caldera-collapse breccias in the San Juan Mountains, Colorado. Geol. Soc. Am. Bull. 87, 1397–1410.
Lipman, P.W., 1984. The roots of ash flow calderas in western North America: windows into the tops of granitic batholiths. J. Geophys. Res. 89, 8801–8841.
Lipman, P.W., 2000. Calderas. Encyclopedia of Volcanoes. Academic Press, San Francisco.
Lipman, P.W., 2007. Incremental assembly and prolonged consolidation of Cordilleran magma chambers: evidence from the Southern Rocky Mountain Volcanic Field. Geosphere 3, 42–70.
Lipman, P.W., Steven, T.A., Mehnert, H.H., 1970. Volcanic history of the San Juan Mountains, Colorado, as indicated by potassium–argon dating. Geol. Soc. Am. Bull. 81, 2327–2352.
MacDonald, W.D., Palmer, H.C., Deino, A.L., Shen, P.-Y., 2012. Insights into deposition and deformation of intra-caldera ignimbrites, central Nevada. J. Volcanol. Geotherm. Res. 245–246, 40–54.
Marocchi, M., Morelli, C., Mair, V., Klötzli, U., Bargossi, G.M., 2008. Evolution of large silicic magma systems: new U–Pb zircon data on the NW Permian Athesian Volcanic Group (Southern Alps, Italy). J. Geol. 116, 480–498.
Marti, J., 1991. Caldera-like structures related to Permo-Carboniferous volcanism of the Catalan Pyrenees (NE Spain). J. Volcanol. Geotherm. Res. 45, 173–186.
Marti, J., 1996. Genesis of crystal-rich volcaniclastic facies in the Permian red beds of the Central Pyrenees (NE Spain). Sediment. Geol. 106, 1–19.
Marti, J., Geyer, A., Folch, A., Gottsmann, J., 2008. A Review on Collapse Caldera Modelling. Elsevier.
Maughan, L.M., Christiansen, E.H., Best, M.G., Gromme, C.S., Deino, A.L., Tingey, D.G., 2002. The Oligocene Lund Tuff, Great Basin, USA: a very large volume monotonous intermediate. J. Volcanol. Geotherm. Res. 113, 129–157.
McCann, T., 2008. Introduction and Overview. The Geological Society, London.
McCann, T., Kiersnowski, H., Krainer, K., Vozarova, A., Peryt, T.M., Oplustil, S., Wetzel, A., Boulvain, F., Dusar, M., Torok, A., Haas, J., Tait, J., Korner, F., 2008. Permian. Geological Society.
McDonough, W.F., Sun, S.-S., Ringwood, A.E., Jagoutz, E., Hofmann, A.W., 1992. Potassium, Rubidium and Cesium in the Earth and Moon and the evolution of the mantle of the Earth. Geochim. Cosmochim. Acta 56, 1,001–1,012.

McLaughlin, R.J.W., 1988. Central Victorian Cauldron Volcanic Province. Geol. Soc. Aust. Spec. Publ. 5.
Mcphie, J., 1986. Evolution of a non-resurgent cauldron: the Late Permian Coombadjha Volcanic Complex: northeastern New South Wales, Australia. Geol. Mag. 123, 257–277.
Morelli, C., Bargossi, G.M., Mair, V., Marocchi, M., Moretti, A., 2007. The Lower Permian volcanics along the Etsch Valley from Meran to Auer. Mitt. Österr. Geol. Ges. 153, 195–218.
Morelli, C., Bargossi, G.M., Marocchi, M., Piccin, G., Moretti, A., Mair, V., 2010. The Athesian Volcanics: a spectacular example of a caldera complex. *85° Congresso*. 85° Congresso SGI, Pisa, Rend. Pisa.
Palmer, H.C., MacDonald, W.D., Gromme, C.S., Ellwood, B.B., 1996. Magnetic properties and emplacement of the Bishop Tuff, California. Bull. Volcanol. 58, 101–116.
Pearce, J.A., Norry, M.J., 1979. Petrogenetic implications of Ti, Zr, Zr, Y, and Nb variations in volcanic rocks. Contrib. Mineral. Petrol. 69, 33–47.
Pearce, J.A., Harris, N.B.W., Tindle, A.G., 1984. Trace element discrimination diagrams for the tectonic interpretation of granitic rocks. J. Petrol. 25, 956–983.
Plant, J.A., Whittaker, A., Demetriades, A., De Vivo, B., Lexa, J., 2005. Geochemical Atlas of Europe Part 1: Background Information, Methodology and Maps. EuroGeoSurveys.
Quick, J.E., Sinigoi, S., Peressini, G., Demachi, G., Wooden, J.L., Sbisà, A., 2009. Magmatic plumbing of a large Permian caldera exposed to a depth of 25 km. Geology 37, 603–606.
Rasband, W., 2011. ImageJ 1.32J ed. National Institutes of Health, USA.
Ring, U., Richter, C., 1994. The Variscan structural and metamorphic evolution of the eastern Southalpine basement. J. Geol. Soc. Lond. 151, 755–766.
Roche, O., Druitt, T.H., 2001. Onset of caldera collapse during ignimbrite eruptions. Earth Planet. Sci. Lett. 191, 191–202.
Rottura, A., Del Moro, A., Caggianelli, A., Bargossi, G.M., 1997. Petrogenesis of the Monte Croce granitoids in the context of the Permian magmatism of the Southern Alps, Italy. Eur. J. Mineral. 9, 1293–1310.
Rottura, A., Bargossi, G.M., Caggianelli, A., Del Moro, A., Visona, D., Tranne, C.A., 1998a. Origin and significance of the Permian high-K calc-alkaline magmatism in the central-eastern Southern Alps, Italy. Lithos 45, 329–348.
Rottura, A., Bargossi, G.M., Visona, D., Tranne, C.A., 1998b. Petrological and geochemical evidence on the origin and significance of the Permian magmatism in the central-eastern Southern Alps, Italy. Mem. Soc. Geol. Ital. 53, 9–21.
Ruffini, R., Borghi, A., Cossio, R., Olimi, F., Vaggelli, G., 2002. Volcanic quartz growth zoning identified by cathodoluminescence and EMPA studies. Microchim. Acta 139, 151–158.
Schaltegger, U., Brack, P., 2007. Crustal-scale magmatic systems during intracontinental strike–slip tectonics: U, Pb and Hf isotopic constraints from Permian magmatic rocks of the Southern Alps. Int. J. Earth Sci. (Geol. Rundsch.) 96, 1131–1151.
Schmincke, H.-U., 1974. Volcanological aspects of peralkaline silicic welded ash-flow tuffs. Bull. Volcanol. 38, 594–636.
Smith, R.L., Bailey, R.A., 1966. The Bandelier Tuff: a study of ash-flow eruption cycles from zoned magma chambers. Bull. Volcanol. 29, 83–104.
Smith, T.R., Cole, J.W., 1997. Somers Ignimbrite Formation: Cretaceous high-grade ignimbrites from South Island, New Zealand. J. Volcanol. Geotherm. Res. 75, 39–57.
Sparks, R.S.J., Walker, G.P.L., 1977. The significance of vitric-enriched air-fall ashes associated with crystal-enriched ignimbrites. J. Volcanol. Geotherm. Res. 2, 329–341.
Sparks, R.S.J., Francis, P.W., Hamer, R.D., Pankhurst, R.J., O'Callaghan, L.O., Thorpe, R.S., Page, R., 1985. Ignimbrites of the Cerro Galan Caldera, NW Argentina. J. Volcanol. Geotherm. Res. 24, 205–248.
Tarling, D.H., Hrouda, F., 1993. The Magnetic Anisotropy of Rocks. Chapman & Hall, London.
Timmerman, M.J., 2004. Timing, geodynamic setting and character of the Permo-Carboniferous magmatism in the foreland of the Variscan Orogen, NW Europe. Geol. Soc. Lond. Spec. Publ. 223, 41–74.
Timmerman, M.J., 2008. Palaeozoic Magmatism. The Geological Society, London.
Visoná, D., Fioretti, A.M., Poli, M.E., Zanferrari, A., Fanning, M., 2007. U–Pb SHRIMP zircon dating of andesite from the Dolomite area (NE Italy): geochronological evidence for the early onset of Permian Volcanism in the eastern part of the southern Alps. Swiss J. Geosci. 100, 313–324.
Walker, G.P.L., 1972. Crystal concentration in ignimbrites. Contrib. Mineral. Petrol. 36, 135–146.
Wang, X., Roberts, J., Schmidt, P., 2001. Flow directions of Carboniferous ignimbrites, southern New England Orogen, Australia, using anisotropy of magnetic susceptibility. J. Volcanol. Geotherm. Res. 110, 1–25.
Whitney, J.A., Stormer, J.C., 1985. Mineralogy, petrology, and magmatic conditions from the Fish Canyon Tuff, Central San Juan Volcanic Field. Colorado. J. Petrol. 26, 726–762.
Whitney, J.A., Stormer, J.C., 1986. Model for the intrusion of batholiths associated with the eruption of large-volume ash-flow tuffs. Science 231, 483–485.
Willcock, M.A.W., Cas, R.A.F., 2014. Primary welding and crystallisation textures preserved in the intra-caldera ignimbrites of the Permian Ora Formation northern Italy: implications for deposit thermal state and cooling history. Bull. Volcanol. 76, 1–16.
Willcock, M.A.W., Cas, R.A.F., Giordano, G., Morelli, C., 2013. The eruption, pyroclastic flow behaviour, and caldera in-filling processes of the extremely large volume (>1290 km^3), intra- to extra-caldera, Permian Ora (Ignimbrite) Formation, Southern Alps, Italy. J. Volcanol. Geotherm. Res. 265, 102–126.
Willcock, M.A.W., Mattei, M., Hasalová, P., Giordano, G., Cas, R.A.F., Morelli, C., 2014. Flow behaviour in the intra-caldera setting: an AMS study of the large (>1290km3) Permian Ora ignimbrite. Geol. Soc. Lond. Spec. Publ. 396, 177–204.
Wilson, C.J.N., Hildreth, W., 2003. Assembling an ignimbrite: mechanical and thermal building blocks in the Bishop Tuff, California. J. Geol. 111, 653–670.
Wolff, J.A., Brunstad, K.A., Gardner, J.N., 2011. Reconstruction of the most recent volcanic eruptions from the Valles caldera, New Mexico. J. Volcanol. Geotherm. Res. 199, 53–68.
Wright, H.M.N., Folkes, C.B., Cas, R.A.F., Cashman, K.V., 2011. Heterogeneous pumice populations in the 2.08-Ma Cerro Galán ignimbrite: implications for magma recharge and ascent preceding a large-volume silicic eruption. Bull. Volcanol. 73, 1513–1533.